Deciphering the mechanisms of photobiomodulation on the blood-brain barrier function in health and disease



Mirriam Domocos

St Catherine's College

University of Oxford

A thesis submitted for the degree of

Master of Science by Research in Physiology, Anatomy, and Genetics

Michaelmas 2025

"Genius is no more than childhood recaptured at will,

childhood equipped now with man's physical means to express itself,

and with the analytical mind that enables it to bring order

into the sum of experience, involuntarily amassed."

- *Charles Baudelaire*

This thesis is dedicated to my parents
whose belief in me, love, and endless encouragement,
made this journey possible.
This achievement is not mine, it's ours.

And to my grandmother, Maria Cipleu,
who passed away from cancer in March 2019.
Everything I work towards is for you.

DECLARATION OF CONTRIBUTION

Hereby, I, Mirriam Domocos, declare that this thesis and all work included within it are entirely my own. This work has not been submitted previously for any other degree at this or another university. The project was carried out by me from October 2024 until January 2026 while I was enrolled as a Master of Science by Research student at the Department of Physiology, Anatomy, and Genetics at the University of Oxford, under the supervision of Dr Mootaz Salman and Professor Francis Szele. A manuscript with the results and findings I generated during my MRes will be prepared and submitted for publication.



Mirriam Domocos

8th January 2026

Word count: 17238

ACKNOWLEDGMENTS

First and foremost, I would like to thank my supervisor Dr Mootaz Salman for taking me on this journey as his MRes student and the continuous mentorship throughout. I clearly remember asking him on my interview day, “Why do you want me in your lab, when other students with more relevant experience applied?”. Dr Salman responded with something I did not expect, “You have passion; that’s something no one can teach!”. I will forever be grateful for this opportunity to dive deeper into my passions, and for his trust, guidance, and support throughout this and other projects.

This thesis would not have been possible without the incredible supervision, support (scientific and personal), and encouragement from my post-doctoral mentor, Dr Luise Schlotterose. Her support went far beyond lab experiments, and I am deeply grateful for her patience, time, and belief in me during challenging moments. I could have not asked for a better supervisor by my side over the past 15 months, and it is truly special to see how our professional relationship grew into a beautiful friendship filled with laughter and support for each other. Thank you, Luise!

A special thank you to Dr Tanya Singh, Dr Luana Campos Soares, and Dr Elisa Marozzi Cruz for their constant help, resources, and advice. It has been an honour to learn from you all and I will cherish our time for years beyond. On that note, I would also like to thank Alice Sartini and Eva Bardol for our time together; two visiting students at the Salman lab who have made my time during long lab hours and weekends much more enjoyable.

I want to thank Professor Francis Szele for his supervision, support, and great advice throughout my MRes. It has been an honour to be part of his lab as my second supervisor and meet the brilliant people in his group. Besides, I want to think him, Dr Luana Campos Soares, and Dr Elisa Marozzi Cruz for trusting me to contribute to their paper within early times of starting my MRes. I have

learned so much from all of them, but most importantly resilience. I want to thank the Szele group for all their advice, help, and shared laughter while I was situated in their office.

I am grateful to the group of Professor Roslyn Bill at the Aston University Birmingham for their scientific input, and to Dr Joe DiDuro, Dr Nagesh Shanbhag, and Professor Denis Bragin for stimulating discussions and continued support during our collaboration. I would also like to thank the Wade-Martins group for welcoming me to their lab, for the access to equipment, and fun socials spent together.

Thank you to the staff and students from St Catherine's College and St Hilda's College for all the unforgettable experiences, incredibly food, financial support, and most importantly the college community. Throughout my time at Oxford, I have met incredible people all across the globe and formed beautiful friendships I will keep close to my heart. A special thank you to SJ, Nafisa, and Kaya, for your open heart, warmth, and words during hard and happy times.

Most importantly thank you to my family, my parents and my three siblings, who are my tower of strength and home. Words could never describe how grateful I am for this opportunity, your sacrifices, faith in me, and the jokes you made to cheer me up. I love you all deeply and would not been here without all of you. Distance is nothing when you carry your people in your heart.

TABLE OF CONTENTS

Abstract *4*

Abbreviations *5*

1. Introduction *9*

1.1. The blood-brain barrier in health **9**

1.2. The blood-brain barrier in disease **12**

1.2.1. Blood-brain barrier dysfunction in hypoxia 12

1.3. Models of the blood-brain barrier **16**

1.4. Photobiomodulation **18**

2. Aims and Objectives *20*

2.1. Overall hypothesis **20**

2.2. Overall aim **20**

2.3. Objectives **20**

3. Methods *21*

3.1. Cell culture **21**

3.1.1. Cell lines 21

3.1.2. Coating of the transwell model 21

3.1.3. Cell seeding and cell count 22

3.1.4. HA seeding 23

3.1.5. HBMEC and HVPC seeding 23

3.2. TEER measurements **25**

3.3. Permeability assay **26**

3.4. PBM treatment 27

3.5. ToxiLight® cytotoxicity assay 29

3.6. AlamarBlue™ cell viability assay 30

3.7. Immunocytochemistry 31

3.8. Quantitative polymerase chain reaction 33

3.8.1. Selection of the housekeeping gene 34

3.9. Small interfering RNA transfection and knockdown 36

3.10. ROS-Glo™ H_2O_2 assay 37

3.11. Seahorse real-time cell metabolic analysis 38

3.12. Proteome profiler human cytokine array 40

3.13. Cell swelling assay 41

3.14. Statistics 42

4. Results 43

4.1. Functional effect of PBM on the BBB in health and disease 43

4.1.1. Coating optimisation 43

4.1.2. PBM restored the barrier function after hypoxia 43

4.1.3. Impact of PBM on tight junction expression 45

4.1.4. Assessment of the cell viability, cytotoxicity, and apparent permeability 46

4.2. Mitochondrial response to PBM 49

4.2.1. Analysis of the mitochondrial respiration 49

4.2.2. Analysis of the glycolytic respiration 53

4.3. PBM reduces oxidative stress 55

4.3.1. Downregulation of ROS upon PBM 55

4.3.2. Dynamics of HIF-1α expression 56

4.4. PBM-mediated downregulation of vWF in HBMECs improves TEER 59

4.4.1. siRNA depletion of vWF confirms its pathway involvement 60

4.5. PBM modulates cytokines and chemokines 61

4.6. Impact of PBM on HAs 63

4.6.1. AQP4 dynamics 63

4.6.2. Expression of the glial fibrillary acidic protein 64

4.7. Impact of PBM on HVPCs 66

4.7.1. Expression of PDGFRβ 66

4.7.2. Dynamics of actin upon PBM 67

5. Discussion 69

6. List of Tables 75

7. List of Figures 76

8. References 81

ABSTRACT

The blood–brain barrier (BBB) is a highly dynamic, multicellular interface that preserves the homeostasis of the central nervous system by regulating molecular exchange between the circulation and neural tissue. BBB disruption is a common feature of acute and chronic neurological disorders, including stroke and neurodegenerative disease, where increased permeability, vascular dysfunction and neuroinflammation contribute to neuronal injury. Hypoxia is a major driver of BBB breakdown, promoting endothelial dysfunction, pro-thrombotic signalling and metabolic failure. Photobiomodulation (PBM), a low-level light therapy, has emerged as a non-invasive approach with reported neuroprotective effects, yet its direct actions on BBB integrity and underlying mechanisms remain poorly defined. Here, we investigated the effects of PBM on BBB function under physiological conditions and following hypoxic injury using a human in vitro BBB model comprising brain microvascular endothelial cells, vascular pericytes and astrocytes cultured in a transwell system. Transient hypoxia (6 hours at 1% O_2) induced a sustained reduction in barrier integrity, which was significantly rescued by PBM at both 24 and 48 hours, as assessed by transendothelial electrical resistance. Mechanistically, PBM modulated distinct but complementary pathways across BBB cell types. In endothelial cells, PBM attenuated hypoxia-associated responses, including downregulation of hypoxia-inducible factor-1α (HIF-1α) and von Willebrand factor (vWF), while enhancing maximal mitochondrial respiratory capacity. In pericytes and astrocytes, PBM reduced reactive oxygen species, consistent with an antioxidant effect. In addition, cytokine profiling revealed suppression of pro-thrombotic signalling following PBM, marked by reduced plasminogen activator inhibitor-1 (Serpin E1/PAI-1) and increased interleukin-8, migration inhibitory factor, and granulocyte macrophage colony-stimulating factor levels. Together, these findings demonstrate that PBM preserves BBB integrity after hypoxic stress by coordinately targeting metabolic, oxidative and thrombo-inflammatory pathways across multiple cell types. By counteracting endothelial dysfunction and restoring vascular homeostasis, PBM represents a promising non-invasive strategy for protecting the BBB in hypoxia-associated neurological disease.

ABBREVIATIONS

2-DG: 2-Deoxy-Glucose

αSMA: Alpha smooth muscle actin

ACs: Astrocytes

AK: Adenylate kinase

AKDR: AK detection reagent

AM: Astrocyte media

Angpt: Angiopoietin

ATP: Adenosine triphosphate

AQP4: Aquaporin-4

BBB: Blood-brain barrier

Bcl-2: B-cell lymphoma-2

Bcl-xL: B-cell lymphoma-extra large

BDNF: Brain-derived neurotropic factor

BS: Blocking solution

BSA: Albumin

CCO: Cytochrome C oxidase

Cld-5: Claudin-5

CNS: Central nervous system

CT: Cycle threshold

CX30: Connexin-30

CX43: Connexin-43

D: Day

DAPC: Dystrophin-associated protein complex

dH_2O: Distilled water

ECAR: Extracellular acidification rate

Abbreviations

ECs: Endothelial cells

EM: Endothelial cell media

FCCP: Carbonyl cyanide-4 (trifluoromethoxy) phenylhydrazone

FDA: Food and drug administration

eNO: Endothelial nitric oxide

GFAP: Glial fibrillary acidic protein

GLUT1: Glucose transporter

GM-CSF: Granulocyte-macrophage colony-stimulating factor

GPCR: G-protein coupled receptor

GROα: Growth-regulated oncogene-α

HAs: Human astrocytes

HDR: High dynamic range

HK: Housekeeping

H_2O_2: Hydrogen peroxide

HBMECs: Human brain microvascular endothelial cells

HVPCs: Human brain vascular pericytes

HIF-1α: Hypoxia-inducible factor-1 alpha

ICC: Immunocytochemistry

IL-1β: Interleukin-1β

IL-6: Interleukin-6

IL-8: Interleukin-8

IL-21: Interleukin-21

IR: Infrared

K^+: Potassium

LLLT: Low level laser therapy

LRP-1: Low-density lipoprotein receptor-related protein-1

MIF: Migration inhibitory factor

Abbreviations

MMP-2: Matrix metalloproteinase-2

MMP-9: Matrix metalloproteinase-9

NO: Nitric oxide

O_2: Oxygen

OCR: Oxygen consumption rate

PBM: Photobiomodulation

PCs: Pericytes

PDGF-BB: Platelet-derived growth factor-BB

PDGFRβ: Platelet-derived growth factor receptor-β

PLL: Poly-L-lysine

PM: Pericyte medium-PLUS

qPCR: quantitative polymerase chain reaction

R/A: Rotenone/Antimycin A

Rgs5: Regulator of G-protein signalling 5

RLU: Relative average luminescence

RPL13A: Ribosomal protein 13A

ROS: Reactive oxygen species

SEM: Standard error of the mean

Serpin E1/PAI-1: Plasminogen activator inhibitor-1

siRNA: Small interfering RNA

TBI: Traumatic brain injury

TEER: Transendothelial electrical resistance

TGF-β: Transforming growth factor beta

TNF-α: Tumour necrosis factor-α

tPA: Tissue-type plasminogen activator

uPA: Urokinase-type plasminogen activator

VCAM: Vascular cell adhesion molecule

Abbreviations

VEGF: Vascular endothelial growth factor

vWF: von Willebrand factor

WPBs: Weibel-Palade bodies

ZO-1: Zonula occludens-1

1. INTRODUCTION

1.1. The blood-brain barrier in health

The human brain is one of the most metabolically active organs and has a specialised vascular network to meet its oxygen (O_2) and nutrient demand, maintaining homeostasis within the central nervous system (CNS). The blood-brain barrier (BBB) is a dynamic and multicellular interface that establishes this tightly regulated vascular system, composed of brain endothelial cells (ECs), that make up the lining of the cerebral blood vessel, with pericytes (PCs) wrapped around them and astrocytes (ACs) that "reach and grab" the vessel. In the brain, ECs are sealed via tight junctions, restricting paracellular transport, and adherens junction, enhancing intracellular adhesion (Wu, Chen et al. 2023, Rust, Yin et al. 2025). The most important tight junctions include occludin and claudin-5 (Cld-5) which link to the cytoskeleton by binding to the tight junction protein zonula occluden-1 (ZO-1) (Figure 1). Other transmembrane proteins like VE-cadherin belong to adherens junction and connect to actin filaments (Mastorakos and McGavern 2019). Furthermore, brain ECs do not possess fenestrations but present themselves with a glycocalyx layer that negatively charges the luminal surface. Thereby, they repel negatively charged molecules and leukocyte adhesion molecules. Altogether, this limits the paracellular and transcellular movement across the BBB and prevents the entry of harmful substances and immune cells, making the CNS immune privileged. To transport wanted substances over the BBB in a bidirectionally manner, ECs express distinct transporters, receptors, and molecular pumps. The glucose transporter (GLUT1) is a carrier-mediated transport and facilitates the influx of one of the most vital nutrients for neurons. In contrast, the low-density lipoprotein receptor-related protein-1 (LRP-1) clears the brain from amyloid-beta via active efflux and allows waste clearance across the BBB (Wu, Chen et al. 2023).

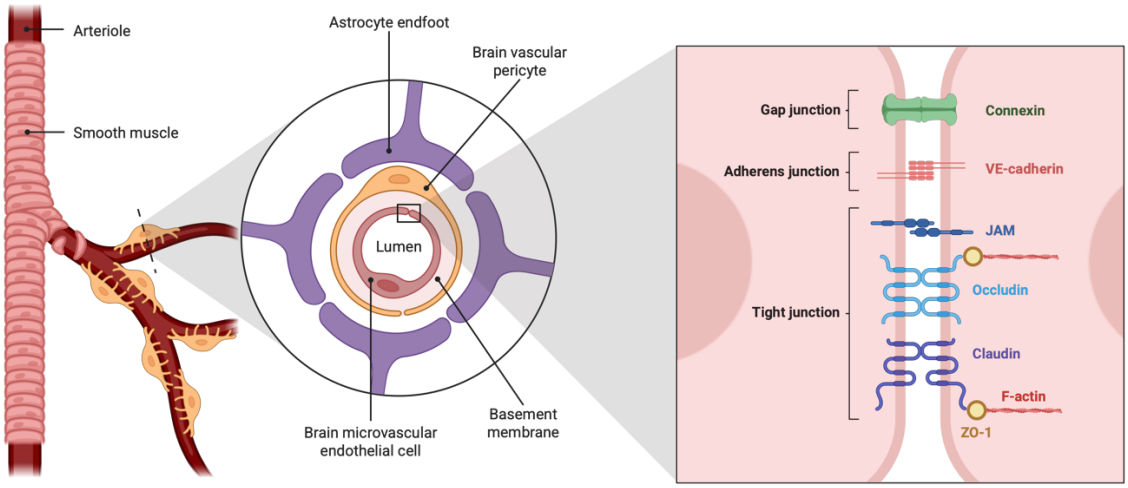


Figure 1: Cellular architecture of the BBB and the junctional proteins contributing to the tightness of endothelial cells at the BBB. Created with Biorender. Adapted from Yang, Wang et al. 2023.

The second cell type of the BBB are PCs, which play a role in providing the structural support, regulating cerebral blood flow and contributing to barrier tightness by forming gap junctions with ECs. They are interlinked by so called "peg-and-socket" junctions that are tightened by N-cadherin and connexin-43 hemichannels (CX43) (Liebner, Dijkhuizen et al. 2018). One of the key factors released from the ECs in the peg-and-socket is the platelet-derived growth factor-BB (PDGF-BB) that binds to its target receptor on the PCs, the platelet-derived growth factor receptor beta (PDGFRβ). Thereby, ECs communicate to recruit more PCs to the blood vessel vital for vessel formation and maintenance of the BBB (Wu, Chen et al. 2023). Apart from other signalling pathways, including the transforming growth factor beta (TGF-β) or angiopoietin (Angpt), PCs are also involved in the contraction of blood vessels. Depending on their localisation and morphology on the vessel, PCs express higher levels of alpha smooth muscle actin (αSMA) to regulate the blood flow and therefore oxygenation to the CNS. Given the importance of PCs, covering around 80% of ECs surface, their loss is directly linked to a reduction of tight junction between ECs and increased permeability (Rust, Yin et al. 2025).

With ACs being the most abundant glial cells in the brain, they play a significant role in the BBB maintenance and neuronal health. They are characterised by their distinct endfeet morphology, with

their flattened extensions “grabbing” and linking to the basement membrane (Salman, Kitchen et al. 2022, Wu, Chen et al. 2023). Similarly to PCs, ACs express gap junction proteins such as connexin-30 (CX30) and CX43 enabling direct cell-to-cell communication for nutrient and ion exchange and regulation of blood flow. This is vital since ACs are in close communication with neurons and form tripartite synapses participating in their synaptic communication and controlling neuronal activity (Araque, Parpura et al. 1999). With their endfeet extension reaching to the vasculature this allows for the neurovascular coupling and maintaining the optimal environment for neurons. Vital for that, is a set of protein complexes found between the endfeet structure and the ECs, the water channel aquaporin-4 (AQP4) (Rust, Yin et al. 2025). AQP4 facilitates bidirectional water movement across the brain and is coupled to the dystrophin-associated protein complex (DAPC) at the endfeet. It is expressed as two main isoforms with translation either starting at Methionine-1, marking the M1 isoform, or at Methionine-23 which creates the shorter isoform M23. While M23-AQP4 forms larger clusters and localises at the endfeet, M1-AQP4 also contributes to AC migration (Verkman, Phuan et al. 2013). Next to water homeostasis, AC also present an inwardly rectifying potassium (K^+) channel Kir4.1 which is facilitates K^+ clearance and is also associated with the DAPC (Nagelhus and Ottersen 2013). Furthermore, transcriptional profiling of perivascular AC identified the enrichment of signalling pathways governing the epithelial to mesenchymal transition, hedgehog signalling, angiogenesis, and matrix adhesion pathways, overall highlighting the functional contribution of AC toward barrier maintenance (Yosef, Xi and McCarty 2020).

1.2. The blood-brain barrier in disease

While neurological and neurodegenerative diseases may vary in their mechanism and phenotype, BBB dysfunction is a hallmark in most of them including Alzheimer's disease, Multiple Sclerosis, stroke and traumatic brain injuries (TBI). Impairments to the BBB lead to its cellular and structural breakdown and thus an increase in permeability, disrupted transport, and infiltration of immune cells. Accordingly, neuroinflammatory pathways are activated, cells start swelling leading to oedema, and ion homeostasis becomes dysregulated. These are all secondary consequences that trigger neuronal damage and cell death (Profaci, Munji et al. 2020). Hypoxia is a known cause for BBB dysfunction and CNS damage as observed in Dementias, epilepsy, and ischemic stroke. Low oxygenation directly impairs the mitochondrial function and energy balance of cells and leads to inflammation. Besides, hypoxia also triggers vascular remodelling and angiogenesis by modulating ECs, hence majorly impacting the health of the BBB (Engelhardt, Patkar and Ogunshola 2014, Merelli, Rodríguez et al. 2018).

1.2.1. Blood-brain barrier dysfunction in hypoxia

One of the first responses to hypoxia is the activation of the hypoxia-inducible factor-1 alpha (HIF-1α) which, in normoxia, is degraded by the ubiquitin-proteasome system. However, in a low oxygenated environment HIF-1α becomes stabile and translocates into the nuclei. Upon the formation of the transcriptional HIF complex, various pathways become active which can either have a protective or pathologic effect such as pro-inflammatory signalling pathways. Given the duration and severity of hypoxia, HIF-1α may mediate a shift from oxidative phosphorylation, an aerobic metabolic mechanism, to glycolysis, an oxygen-independent respiratory pathway (Merelli, Rodríguez et al. 2018). Yet, the adenosine triphosphate (ATP) yield from glycolysis may not be sufficient to adapt to the cell's energy demand leading to cellular stress and dysfunction. In addition, hypoxia contributes to mitochondrial dysfunction which can manifest in the upregulation of reactive oxygen species (ROS) causing oxidative stress (Kim, Tchernyshyov et al. 2006). To adapt to the decreased energy production and low oxygenation, HIF-1α additionally activates angiogenic and

erythropoietic pathways to facilitate new vessel formation and oxygenation. This involves the upregulation of the matrix metalloproteinase-2/9 (MMP-2/9) to degrade extracellular matrix proteins and the expression of the vascular endothelial growth factor (VEGF) to induce vascular growth. With MMPs degrading proteins, they also target tight junction proteins of ECs if regulated aberrantly. Interestingly, two-photon microscopy of mice after photo-thrombotic occlusion revealed, that MMP activation particularly concentrates at the soma of PCs with dynamic changes of tight junctions (Liebner, Dijkhuizen et al. 2018). Furthermore, *in vivo* studies have shown, that VEGF can also induce BBB impairment through induced ECs fenestrations and caveolae (Roberts, Delaat et al. 1998, Liebner, Dijkhuizen et al. 2018). Considering mitochondrial stress, ROS production, and MMP upregulation, the BBB becomes leaky due to loss and altered localisation of ZO-1, Cld-5, and occludins. Therefore, hypoxia is highly associated with BBB dysfunction and infiltration of blood molecules such as leukocytes driving inflammation (Ogunshola and Al-Ahmad 2012).

Damage to the BBB and CNS activates the release of cytokines, like interleukin-6 (IL-6) and tumour necrosis factor-alpha (TNF-α), chemokines, and adhesion molecules to facilitate the recruitment of leukocytes (Andjelkovic, Situ et al. 2023). Next to the vascular cell adhesion molecule (VCAM), ECs upregulate the platelet-adhesion molecule von Willebrand factor (vWF) which is normally stored in Weibel-Palade bodies (WPBs). Upon release, vWF mediates the attachment of platelets to the endothelium, facilitate leukocyte infiltration, and favours the formation of platelets. This response is highly associated with inflammation and hypoxia with severe impacts to the BBB health. Upregulation of vWF is thought to downregulate Cld-5 levels and interacts with the expression of LRP1 during inflammation, which leads to waste accumulation in the brain (Kawecki, Lenting and Denis 2017). Other pro-thrombotic responses of ECs include the release of the plasminogen activator inhibitor (Serpin E1/PAI-1) that blocks plasminogen activators (PA) such as the urokinase-type (uPA) and tissue-type (tPA). This orchestrated response favours coagulation after hypoxia, harms the endothelium, and is attributed to EC dysfunction (Kutikhin, Shishkova et al. 2022).

Even though ACs and PCs are thought to be more resilient towards hypoxia, they still respond with the activation of the HIF pathway and downstream elements including expression of MMPs and VEGF. Though, ACs possess a higher metabolic capacity to adapt to hypoxia by relying on glycolysis and avoiding mitochondrial stress. Nevertheless, ACs are one of the most immune-active cells and synthesise an array of cytokines such as interleukin-1β (IL-1β) and monocyte chemoattractant proteins in response to HIF-1α. This activation of leukocyte attractants works in conjunction with the adhesion molecules released from ECs and impair the tight junction distribution (Engelhardt, Patkar and Ogunshola 2014). With ACs becoming active they "retract" their end-feet and delocalise AQP4 around the cell soma. The cellular stress, coming from hypoxia, leads to an impaired Na^+/K^+-ATPase activity and thus an osmotic imbalance that drives water retention in ACs. With AQP4 being delocalised, ACs start to swell and cause cytotoxic oedema, a phenotype commonly observed after hypoxia. Loss of perivascular AQP4 is also associated with a reduced glymphatic output and waste retention in the CNS (Dunn and Isaacs 2021, Salman, Kitchen et al. 2022).

Next to HIF-1α activation, MM-2/9 secretion, and immune responses e.g., TNF-α and IL-6, PC react to hypoxia with the expression of the regulator of G-protein signalling 5 (Rgs5). Rsg5 act independent of HIF-1α and negatively regulates the G-protein coupled receptor (GPCR) as a GTPase activating protein. Besides, Rgs5 activated migration of PC away from the basal membrane leaving the EC unsupported (Carlsson, Enström and Paul 2023). When considering the impact of severe hypoxia on PC, it is important to consider the structural and physiological role of them in maintaining the BBB. The loss of EC-PC interaction is directly linked to the loss of tight junctions and an increase in BBB leakiness (Engelhardt, Patkar and Ogunshola 2014). Further downstream effects of Rgs5 include the desensitisation of PC to PDGF-BB by limiting the phosphorylation of PDGFRβ. Thereby, PC recruitment is limited and attempts to support the endothelium after hypoxia fail. With the loss of PC and remodelling of EC monolayer, the BBB is becomes dysfunctional

characterised by an increased permeability, aberrant transport, and low cerebral blood flow (Engelhardt, Patkar and Ogunshola 2014, Carlsson, Enström and Paul 2023).

1.3. Models of the blood-brain barrier

Given the disease implications of the BBB and potential to manage neurological and neurodegenerative diseases by modulating the BBB integrity, studying the BBB via *in vitro* models is highly favourable. *In vitro* models have various advantages over *in vivo* models that include establishing a controlled cellular environment, easy reproducibility, less ethical concerns, adaptation of the model to the biological question, and allowing follow-up assays to study cell behaviours. Moreover, by using human brain primary cell lines or human derived pluripotent stem cells differentiated into BBB cells, the modelling of BBB breakdown and cellular mechanisms become more accurate and physiologically relevant (Simöes Da Gama and Morin-Brureau 2022). *In vitro* models of the BBB can be grossly divided into static and dynamic models which are characterised by an induced shear stress. Such models use microfluidic systems mimicking the blood flow in either a 2D culture or a 3D cellular architecture of a blood vessel. Yet, apart from their physiological relevance, alike models do not allow for further monitoring and analysis of cells including immunocytochemistry or gene expression analysis (Cader 2022). The static transwell model makes use of a porous membrane to compartmentalise the system into a two-chamber setup. The upper or basal chamber represents the lumen of the vessel and the lower or apical chamber the parenchyma. Accordingly, ECs are cultured on the basal side, forming the monolayer of the BBB model, with PCs and ACs cultured on either side of the membrane to allow for direct cell-to-cell contact. Given its reproducibility and high-throughput capacity, it is the gold standard for modelling barrier properties and permeability studies in drug discovery (Gokce, Altun et al. 2025). In addition, by using the transwell model, cells can be seeded in various forms of cultures based on the biological question. The follow-up experiments to investigate the signalling pathways, permeability, and immunochemistry can give scientists a greater understanding of cellular and molecular mechanisms (Simöes Da Gama and Morin-Brureau 2022). One of the most insightful measures to understand the barrier function, is the transendothelial electrical resistance (TEER) which is the ionic conductance of paracellular diffusion in an endothelial monolayer. The electrical resistance is measured by

placing two electrodes, with one being placed in the upper and the other in the lower chamber of the transwell model and calculated according to Ohm's law (Resistance [ohm] = Voltage [volt] / Current [amps]). To calculate the TEER the ohmic resistance of a blank transwell needs to be subtracted of the ohmic resistance of a monolayer. Moreover, the model's area proportionally impacts the TEER ($\Omega \cdot cm^2$) and thus will be multiplied with the referenced ohmic resistance (Waithe, Peng et al. 2024). Other factors affecting the TEER include the environmental temperature, instrument, composition and ions of culture medium, type of membrane, and pore size (Srinivasan and Kolli 2025). With models using different cell types, pore sizes, ranging from 0.4 mm to 3 mm, and transwell sizes from 6- to 96-well inserts, TEER measurements vary accordingly. Standardisation across models is limited and comparisons of TEER between research studies needs to be done carefully taking into account all variabilities (Gokce, Altun et al. 2025).

1.4. Photobiomodulation

Photobiomodulation (PBM) is a non-invasive, low level laser therapy (LLLT) with light ranging from 600 to 1100 nm. The red and infrared light triggers a cascade of beneficial chemical, molecular, and behavioural changes within the cell. Such downstream pathways include neuroprotective effects, boosted cell metabolism, and increased blood flow, while decreasing oxidative stress and inflammation (Huang, Hamblin and Zhang 2024). In depth, the photons of the red and infrared light get absorbed by the fourth terminal enzyme of the electron transport chain in the mitochondria, the cytochrome C oxidase (CCO). With the activation of CCO, PBM increases the number of available electrons to reduce molecular oxygen. This enhances the mitochondrial membrane potential and ATP levels produced by the mitochondria (Hennessy and Hamblin 2017). In addition, PBM dissociated the nitric oxide (NO) bound to the haem iron and cooper centre of the CCO, thus elevating endothelial NO (eNO) and cerebral blood flow. Indeed, a clinical study found improved regional cerebral blood flow in 66.7% of individuals treated with pulsed PBM following a TBI (Hipskind, Grover et al. 2019). To establish a greater electron gradient, PBM also supports the conversion of O_2 into water thus modulating O_2 free radicals and ROS levels. While studies found that PBM impacts ROS levels in both directions, there seems to be a dependence on the cell's state of existing oxidative stress where PBM lowers ROS synthesis to protect the cellular health. On the contrary, elevating ROS levels in homeostasis can support crucial cell proliferation and repair pathways (Yan, Zhou et al. 2025).

So far PBM has shown its effectiveness in managing pain for instance for sports injuries, within dermatology to treat arthritis or skin inflammation, and in wound healing and repair. One great example of its use is in promoting tissue function and wound regeneration of mucositis for patients who underwent cancer treatments. With very few side effects PBM has been approved for pain relief as a medical device by the U.S. Food and Drug Administration (FDA). Given its therapeutic power, PBM has gained much attention and interest for neurorehabilitation and improving cognitive

function after TBI, stroke, or in neurodegenerative diseases (Enengl, Hamblin et al. 2020, Chamkouri and Chen 2025). Indeed, a study found that cognitive deficits and anxiety-like behaviours reversed upon PBM irradiation in APP/PS1 transgenic *in vivo* model mimicking Alzheimer's disease. Moreover, they also reported upregulation of Cld-5, ZO-1, and occludin restoring the BBB integrity while facilitating the clearance of amyloid-beta plaques via LRP1 (Ma, Ye et al. 2025). Another review assessed the clinical relevance of PBM on endothelial dysfunction and revealed, that PBM improved the recovery of patients after coronary intervention and prodromal complications in saphenectomy after a myocardial revascularisation. Most likely by maintaining the endothelium and modulating eNO and TGF-β levels. Besides, inflammation was lowered as a result of PBM's antioxidant power and blood pressure levels dropped after hypertension. It was also reported, that PBM improved cognitive function after ischemia by restoring the brain's microvasculature. Altogether, PBM has shown its potential serving as a non-invasive, effective, and affordable therapeutic strategy to improve cell function and promote healing (Colombo, Signore et al. 2021). Despite the great evidence on *in vivo* work and clinical assessments, publications that investigate the cell-specific effects of PBM on the BBB and on molecular level are limited. Some publications have assessed the effect of PBM on EC monolayers, mimicking the microvasculature, or on a wild-type BBB but not in the context of a hypoxia-stressed or damaged BBB. There have also been no reports on the impact of PBM on brain microvascular PCs in health and disease. Moreover, even though the transwell model offers a great platform to study the effect of PBM there are only a handful of projects working with this method.

2. AIMS AND OBJECTIVES

2.1. Overall hypothesis

PBM boosts mitochondrial function, restores cellular health, and improves vascular function, therefore it could be used as a therapeutic strategy to limit BBB breakdown, reduce permeability, and thus prevent neuronal cell death in neurological and neurodegenerative diseases.

2.2. Overall aim

The aim of this thesis is to define how PBM influences BBB function under physiological conditions and to elucidate the mechanisms by which it restores barrier integrity following hypoxic injury, thereby evaluating its therapeutic potential.

2.3. Objectives

a. To establish a physiologically relevant *in vitro* model of the BBB using human cell lines.
b. To assess the functional impact of PBM on the healthy BBB model.
c. To investigate changes in mechanisms and cellular behaviour following hypoxia to draw a conclusion on its impact on the BBB.

3. METHODS

3.1. Cell culture

3.1.1. Cell lines

Immortalised (SV40 antigen T) human brain microvascular endothelial cells (HBMECs) (Innoprot; P10361-IM), human astrocytes (HAs) (Innoprot; P10251-IM), and human brain vascular pericytes (HVPCs) (Innoprot; P10363-IM) were purchased commercially from Innoprot and used up to passage number 20. The cells were thawed from the liquid nitrogen storage in a 37°C pre-warmed water bath for around 1-2 minutes. Before cells were fully thawed, 1 mL of appropriate media was carefully pipetted into the vial, drop-by-drop. Then the cells were added into an uncoated 75 cm^2 flask (Corning; 430641U) containing 12 mL of the appropriate media. HBMECs, HAs, and HVPCs were always seeded at a density of 2.6×10^4 cells/cm^2 and maintained in either endothelial cell medium (EM) (Innoprot; P60104), astrocyte medium (AM) (Innoprot; P60101), or pericyte medium-PLUS (PM) (Innoprot; P60121-Plus) respectively. Media was fully changed every other day until the flask reached a confluence of 80-90% when cells were splitted and passaged.

3.1.2. Coating of the transwell model

All *in vitro* models (Figure 2A) were seeded on the 24-well plate hanging inserts from Millipore (PTSP24H48) with a pore size of 3 µm and a surface area of 0.3 cm^2. To facilitate cell adherence and optimal growth, the transwells were coated with 200 µL Geltrex™ (Thermo Scientific; A1413302) in the apical chamber and Poly-L-lysine (PLL) (Sigma-Aldrich; P4705), with a concentration of 2 µg/cm^2 diluted in distilled water (dH_2O), on the basal side of the membrane. The PLL coating was carried out first on day 1 (D1) by inverting the insert resting in the cover plate (Figure 2B). For each membrane with an area of 0.3 cm^2, 50 µL of PLL was pipetted and the lid of a 24-well plate carefully placed on top. This allowed an even and flat distribution of the PLL coating. Inserts were set aside at room temperature for an hour followed by the seeding of HAs.

The apical chamber was coated with Geltrex on D2 of the cultivation process. Before the Geltrex was fully thawed, slowly from -80°C, 1 mL of cold EM was slowly pipetted to the Geltrex and mixed. The full content was added to a falcon containing 49 mL of cold EM and mixed by inversion. 200 µL of the Geltrex mixture was quickly pipetted into each apical chamber of PLL coated inserts. For that, inserts were placed inside the wells of a 24-well plate. Once coated, inserts were incubated at 37°C for an hour followed by the seeding of HBMECs and HVPCs. To prevent gelation in the falcon the prepared Geltrex was stored at -4°C and kept on ice during the coating process.

3.1.3. Cell seeding and cell count

HAs were seeded on D1 following the PLL coating and HBMECs and HVPCs on Geltrex-coated inserts on D2. All cells were lifted the following protocol. Once flask has reached an 80-90% confluence, the cells were washed with 7 mL PBS (Gibco; 10010023) and lifted with 3 mL TrypLE (Gibco; 12605-013) at 37°C for 3 minutes. To stop the enzymatic activity of TrypLE, 4 mL of warm cell culture media was added to the flask. Cells were carefully rinsed off the flask without creating bubbles. Once cells were rinsed off, the 7 mL of lifted cells were added to a 15 mL falcon and centrifuged for 4 minutes at 185 rcf. The supernatant was discarded, and the pellet resuspended in 1 mL warm cell culture media. 10 µL were pipetted into a cell counting chamber and counted with the Countess 3 Automated Cell Counter (Invitrogen). The cells were then diluted with the appropriate cell culture media based to reach the desired cell count (Table 1).

	Cell count per transwell insert [cells/insert]		
TRANSWELL CULTURES	HAs	HBMECs	HVPCs
Monocultures	15,000	100,000	25,000
HA/HBMEC Co-culture	15,000	100,000	-
HA/HVPC Co-culture	15,000	-	25,000
HVPC/HBMEC Co-culture	-	75,000	25,000
Tri-cultures	15,000	75,000	25,000
Blank	-	-	-

Table 1: Cell count of seeded HAs, HBMECs, and HVPCs per 24-well transwell insert (cells/insert) for all cultured transwell models.

3.1.4. HA seeding

Before seeding the HAs, the remaining PLL was aspirated and the coating washed with PBS once. The inserts were still placed inverted on the cover. Per insert, 20 µL of diluted HAs were pipetted and distributed equally on the washed PLL coating, making sure the entire membrane is covered with cells (Figure 2B). For cultures without HAs 20 µL of AM was pipetted instead and distributed respectively. The bottom of the 24-well plate was now carefully placed over the inserts facing down. It was therefore important to place inserts precisely to not damage either the coating or the cells. Once placed, the plate was incubated at 37°C for 2 hours to allow the attachment of HAs. The plate was then turned around, with the basal side facing downwards, and 1.3 mL warm AM added to the well followed by an incubation at 37°C overnight.

3.1.5. HBMEC and HVPC seeding

After the apical coating, the remaining Geltrex was aspirated. Per insert, 100 µL of either diluted HBMECs, HVPCs, or both were pipetted drop-by-drop into the apical chamber onto the coating. Cells were topped up with appropriate media following table 2 with a total volume of 500 µL in the apical chamber (Figure 2B). The plate was incubated at 37°C and media was fully changed for both compartments every other day until D8 of the cultivation timeline.

Cell culture media

TRANSWELL CULTURES	Apical chamber [500 µL]	Basal chamber [1.3 mL]
HBMEC Monocultures	EM	AM
HA Monocultures	AM	AM
HVPC Monocultures	PM	AM
HA/HBMEC Co-culture	EM	AM
HA/HVPC Co-culture	PM	AM
HVPC/HBMEC Co-culture	EM:PM (1:1)	AM
Tri-cultures	EM:PM (1:1)	AM
Blank	EM:PM (1:1)	AM

Table 2: Cell culture media for apical and basal chamber for each transwell culture.

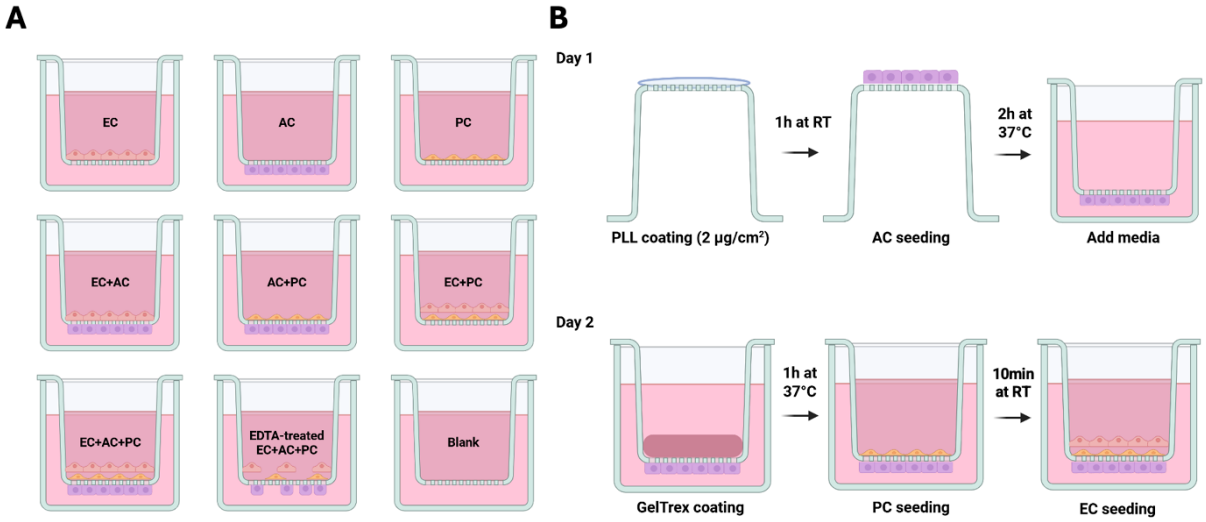


Figure 2: Illustration of (A) the cultured in vitro transwell models, to understand cell-to-cell communication, and (B) the coating and seeding of a tri-culture model. Created with Biorender.

3.2. TEER measurements

To calculate the TEER, the resistance was measured with the EVOM^{TM} Manual Meter (World Precision Instruments; EVM-MT-03-02) and handling was in accordance with the manual and protocol. All measurements were done in a sterile hood, and electrodes were always carefully prepared. The EVOM was blanked with a cell-free but coated transwell and the resistance of each transwell measured. The electrodes were carefully placed on the transwell with the shorter electrode in the transwell insert and the longer electrode outside the transwell. It is critical that both electrodes are immersed in enough media and placed at the middle of the transwell, not touching any walls. To maintain consistent measurements of the resistance, the electrodes were placed in the same manner for each transwell using an electrode placement frame. Once correctly placed, the resistance was captured after 3 to 7 seconds for the electrodes to adjust. For a negative control of disrupted TEER, 50 µL EDTA (0.5 M) (Invitrogen; 15575-020) was added to a separate cultured tri-culture. At each time point and for each transwell culture, three separated resistance measurements with individually adjusted blanks were recorded. The resistance was then multiplied by the area of the membrane ($0.3cm^2$) to calculate the TEER. The TEER was then averaged and taken relative to the baseline TEER calculate the change in relative TEER. The measurements were taken in four biological replicates with three technical replicates per biological.

3.3. Permeability assay

The barrier integrity was analysed using a permeability assay measuring the amount of 10 kDa Dextran passaging trough the cell layer. The apparent permeability (Papp) is a measure of diffusion over time and another method to investigate the barrier function. For that, the diffusion of a fluorescent tracer molecule from the apical to the basal compartment get detected over time. Each transwell contained 500 µL of the appropriate media in the apical compartment and 1.3 mL of PBS in the basolateral compartment. For timepoint zero, 100 µL PBS of the basolateral compartment was sampled into a black-walled, clear-bottom 96-well microplate. Then 2 µL Dextran Alexa Fluor 488 10kDa (5 µg/mL) (Invitrogen; D22910) was mixed well in the apical compartment of each transwell. Every volume taken for sampling was replaced with 100 µL PBS. Samples were respectively taken after 5, 10, 15, 20, 25, 30, and 60 minutes and topped up with 100 µL PBS in-between. The fluorescence signal was firstly measured at excitation/emission of 495/519 nm with the CLARIOstar microplate reader after 30 minutes and after completing the final sampling at 60 minutes. The measurements were taken in four biological replicates.

The calculation of the Papp (cm/s) was based on the formula to the right (Barberio, Withers et al. 2022). To estimate the LY, which is the concentration of dextran in the basal (LY_B) and apical (LY_A) compartments, a standard curve was done ($y = 994{,}118.167*x - 134{,}938.85$; $R^2 = 0.9998$). Vol_A and Vol_B are the volumes for both compartments and T (seconds) the time of incubation. The starting concentration of the dextran tracer added on the apical side is shown as C and A is the membrane area.

$$P_{app} = \frac{\left[\frac{Flux \times Vol_B}{T}\right]}{\left[\frac{1}{A \times [C]}\right]} \quad where\ Flux = \frac{LY_B \times Vol_A}{LY_A \times Vol_B} \times 100$$

3.4. PBM treatment

The tropwrap TW-03B (Figure 3) from ProNeuroLight was used throughout the project since it is already a clinically relevant and available PBM light source. It also has an advanced dual chip LED technology to emit light in four wavelengths simultaneously. The topwrap is 20 cm in length and 10 cm in width and has 9 rows of 5 LED lights, alternating in their dual chip combination. There were 12.5 dual chips, with one emitting red light at wavelength 635 nm and the other emitting infrared (IR) light at 904 nm. The other 10 dual chips emitted light at IR at 810 nm and 1064 nm.

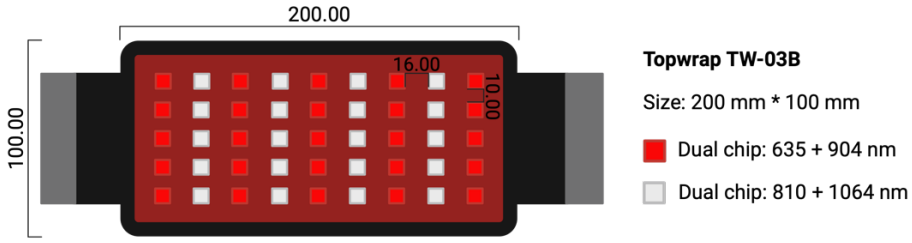


Figure 3: LED lights and dimensions of the topwrap TW-03B from ProNeuroLight used for the PBM treatments. Created with Biorender.

SOURCE	LED1	LED2	LED3	LED4	TOTAL
Wavelength (nm)	635 (RED)	810 (IR)	1064 (IR)	904 (IR)	-
Number of LED	12.5	10	10	12.5	45
Total power (mW)	333.75	191.1	537.8	337.88	1400.53
Irradiance per LED (mW/cm^2)	212.58	152.15	428.18	215.21	-
Total irradiance power (mW/cm^2) at 10 cm	26.57	15.21	42.82	26.90	111.51
Total fluence delivered over the entire therapy (J/cm2)	797.17	456.45	1284.55	807.03	3345.20
Total dose delivered over the entire therapy (Joules)	100.13	57.33	161.34	101.36	420.16

Table 3: Properties of each LED light found in the toprwap TW-03B for one session lasting 5 minutes.

One 24-well plate with the transwells was irradiated from below to mimic the light reaching the BBB from the basal side. One PBM treatment included 3 cycles of 5 minutes with a recovery period of 1 hour in-between at 37°C, based on existing literature (Winter, Dungel et al. 2018, Zhou, Ohulchanskyy and Qu 2021, Staelens, Di Gregorio et al. 2022). The topwrap was on for around 2 minutes before treatments to allow it to reach the desired power. The plate was placed at 10 cm above the flat-laid topwrap on two tip boxes which were appropriately sterilised beforehand. During treatments, the main light was switched off and the procedure carried out away from the window.

3.5. ToxiLight® cytotoxicity assay

The ToxiLight Non-Destructive Cytotoxicity BioAssay Kit (Lonza; LT17-217) was used to directly detect changes in cell death after hypoxia. Upon cell damage, the enzyme adenylate kinase (AK) get released from all eukaryotic cells in the culture medium. The AK helps forming ATP which gets detected using a bioluminescent luciferase reaction. Changes in oxygenation including oxygen deprivation and reoxygenation may impact AK levels and therefore the assay outcome. With hypoxia impairing the mitochondrial function, the AK levels may also be affected during oxygen deprivation. The assay was carried out following the manufacturers protocol with all reagents included in the assay kit. At 48 hours post-treatment, 50 µL of the cell supernatant from each insert was taken before the alamarBlue assay was done. The assay buffer and lyophilized AK detection reagent (AKDR) were brought to room temperature prior to reconstituting the AKDR in 10 mL assay buffer. While the AKDR was equilibrating for 15 minutes, 20 µL of cell supernatant was transferred to a white 96-well plate with clear bottoms for luminescence with two technical replicates per sample. 100 µL of AKDR was added to each well and incubated for 5 minutes. The luminescence was measured with the CLARIOstar PLUS microplate reader (BMG Labtech) and the relative average luminescence (RLU) calculated by dividing the luminescence of samples to the of their according cell-free media. To calculate the relative luminescence the endpoint RLU was divided by the baseline RLU. The assay was measured in four biological replicates.

3.6. AlamarBlue™ cell viability assay

The cell viability was assessed using the alamarBlue™ reagents (Invitrogen; DAL1025) as it is not an endpoint assay and does not require cell lysis. Viable cells convert the non-fluorescence indicator dye Resazurin to the highly fluorescent compound Resorufin by reduction which is directly proportional to cell viability. The assay was carried out before the exposure of transwell cultures to PBM or hypoxia and 48 hours after. Changes in oxygenation including oxygen deprivation and reoxygenation may impact the rate of Resazurin reduction and therefore the assay outcome. For that, 10% of either the apical and basal volume of the alamarBlue dye was pipetted to the appropriate compartment and mixed by pipetting. For a volume of 500 µL in the apical chamber and 1300 µL in the basal chamber, respectively 50 µL and 130 µL of the alamarBlue dye was used for each culture. The cultures were then incubated for 2 hours at 37°C. Next, samples of the apical and basal chambers were pipetted into a black 96-well microplate and the fluorescence measured. The sample volume was 10% of either the apical and basal volume. After the measurements, transwells were washed with PBS and new, warm media added according to table 2. The fluorescence was measured at excitation/emission of 495/519 nm with the CLARIOstar microplate reader and the relative fluorescence signal calculated by taking the average of the fluorescence from both compartments, after subtracting the background signal from the blank (the media), relative to the baseline fluorescence signal before any conditioning. The assay was measured in four biological replicates.

3.7. Immunocytochemistry

The transwell cultures were stained for certain proteins and DAPI was used as a nuclear marker to analyse expression and localisation patterns. For the first step of the immunocytochemistry (ICC) the media was aspirated from both transwell compartments and then washed with PBS. Cells were fixed with 300 µL and 150 µL of 4% formaldehyde, diluted in PBS, (Thermo Scientific; 28908) in the basolateral and apical compartment respectively. After 15 minutes, the formaldehyde was thoroughly aspirated and washed with PBS. Cultures were topped up with 1 mL PBS, sealed with parafilm and stored at 4°C for immunocytochemistry.

After fixation, transwells were washed twice with PBS for 5 minutes and permeabilised with 0.3% Triton X-100 (Invitrogen; HFH10) in PBS for 10 minutes at RT. Cells were then washed twice again and incubated with blocking solution (BS) (0.5% BSA (Sigma-Aldrich; A8806-1G), 0.5% Glycine (Sigma-Aldrich; G8898-500G)) for 1 hour at RT. Primary antibodies (Table 4) were diluted appropriately in BS and cells incubated in both compartments at 4°C overnight. Transwells were washed with PBS twice for 10 minutes before incubation with the secondary antibodies (Table 4) and DAPI (Invitrogen; D1306) (0.8 µL per 1 mL) diluted in BS for 1.5 hours. After washing with PBS twice for 10 minutes, membranes were carefully cut out with a scalpel along the edge and mounted with Fluoromount (Millipore; 345789) on a coverslip. Cells were imaged with the 3i Marianas Confocal Microscope (Intelligent Imaging Innovations) at 63X and analysed via Fiji Image J 1.54p with Java 21.0.7 (64-bit). For each culture three biological replicates were stained and three images taken per biological. For quantitative analysis, the average of either the mean intensity, the mean intensity co-localised with DAPI, or the area normalised to the DAPI cell area was taken from the three representative images.

ANTIBODY	HOST	DILUTION	CATALOG NUMBER	SUPPLIER
ZO-1	Rat	1:200	15652	Cell Signaling
vWF	Sheep	1:400	ab11713	Abcam
AQP4	Rabbit	1:200	ab128906	Abcam
GFAP	Rat	1:500	13-0300	Invitrogen
PDGFRb	Rabbit	1:200	MA5-15143	Invitrogen
HIF-1a	Mouse	1:200	MA1-516	Thermo Scientific
Actinred™ 555	-	2 drops/mL	R37112	Life Technologies Ltd
Anti-Sheep 647	Donkey	1:1000	A21448; LOT: 2720396	Invitrogen
Anti-Rat 488	Donkey	1:1000	A21208; LOT: 2668657	Invitrogen
Anti-Mouse 555	Donkey	1:1000	A31570; LOT: 3034154	Invitrogen
Anti-Rabbit 647	Donkey	1:1000	A31573; LOT: 2997084	Invitrogen
Anti-Mouse 488	Donkey	1:1000	A2120; LOT: 3006753	Invitrogen

Table 4: Primary and secondary antibodies used for staining of HBMECs, HVPCs, and HAs.

3.8. Quantitative polymerase chain reaction

To quantify the RNA expression of selected genes, the RNA was extracted from all cell types and cDNA generated, followed by a real-time quantitative polymerase chain reaction (qPCR) assay. HBMECs, HVPCs, and HAs were seeded in 12-well plates (3.0 x 10^5 cells) and cultured to a confluency of 80% before being exposed to treatment and dry frozen after 48 hours. Total RNA was extracted with a TRIzol (Zymo; R2050-1-200) and purified with the commercially available Direct-zol RNA MicroPrep kit (ZYMNO Research; R2062). To generate cDNA 20 µL (500 ng), 1 µL Random Primers (1:20) (Invitrogen; 48190011) and 1 µL 10 mM dNTP mix (Invitrogen; 18427089) were mixed with the purified RNA and appropriate volume of dH_2O for a final volume of 13 µL. This was incubated at 65 °C for 5 minutes followed by 4°C for at least 1 minute. Then, 1 µL RnaseOUT Recombinant Ribonuclease Inhibitor (40 U/µL) (Invitrogen; 10777019) and 4 µL 5X First Strand Buffer, 1 µL 0.1 M DTT, and 1 µL SuperScript III RT (200 U/µL), all three included in the SuperScript III RT kit (Invitrogen; 18080093), were gently added and incubated at 65°C for 5 minutes followed by 55°C for 60 minutes and 70°C for 15 minutes. For one qPCR reaction (20 µL), 10 µL 1x Fast SYBR Green Master Mix (Applied Biosystems; 4385612), 1 µL of each the relevant forward and reverse primers (0.2 µM), 5 µL of cDNA (1:10), and 3 µL dH_2O were mixed. The comparative cycle threshold (CT) values were detected with the QuantStudio 3 Real-time PCR System (Applied Biosystems; A28567) and the qPCR data was analysed following the $2^{-\Delta\Delta CT}$ method normalising to the untreated normoxia cells as the control. The assay was measured in four to six biological replicates.

RPL13A used as the housekeeping (HK) gene with the following primers: forward 5' GGTCCTGGTGCTTGATGGTC 3', reverse 5' GGCCCAGCAGTACCTGTTTA 3'. In general, all primers were ordered from IDT (Integrated DNA technologies) and custom designed using Primer-BLAST with 1) a melting temperature around 59°C ± 1°C, 2) a GC content ranging from 50% to 55%, and 3) an amplicon size of 70 to 200 base pairs (table 5).

	Primer Sequence (5'→3')	
PRIMERS	Forward Primer	Reverse Primer
RPL13A	GGTCCTGGTGCTTGATGGTC	GGCCCAGCAGTACCTGTTTA
ZO-1	CCGCGGAGTTTCGGGTC	TCCTCCATTGCTGTGCTCTTG
vWF	GCTCATGCAACATCTCCTCTG	ACTCACACAAAGTCTTCTCACA
PDGFRb	CCACACTCCTTGCCCTTT	CACAGACTCAATCACCTTCCA
α-SMA	AAAAGACAGCTACGTGGGTGA	GCCATGTTCTATCGGGTACTTC
Rgs5	GAGTTGAAGAGCAAAACCAAGTG	CTGAAGATATCCAGACAGTGCT
AQP4	AGGCAATGAGAGCTGCAC	AAGCCACCATGATGTTCTCT
GFAP	CCTGCAGATTCGAGAAACCA	CCTGCTTGGACTCCTTAATGAC
IL-6	GCAGATGAGTACAAAAGTCCTGA	TTCTGTGCCTGCAGCTTC
HIF-1a	ATCACCCTCTTCGTCGCTTC	GGAAAGGCAAGTCCAGAGGT

Table 5: Forward and reverse sequences for all primers used in 5' to 3'.

3.8.1. Selection of the housekeeping gene

Exposing cells to hypoxia significantly alters their metabolism and thus expression of HK genes. An appropriate screening of potential HK genes was required to identify a stable candidate. In total, the CT values for nine genes (*GAPDH, 18S RNA, CDKN1B, PPIA, RPL13A, RRP1, B2M, TBP, HPRT1*) were determined via qPCR of HBMECs, HVPCs, and HAs in all conditions. The genes were selected from available literature that reported potential HK genes (Table 6).

	Primer Sequence (5'→3')		
GENES	Forward Primer	Reverse Primer	PMID
GAPDH	ACATCGCTCAGACACCATG	TGTAGTTGAGGTCAATGAAGGG	-
18S RNA	GAGACTCTGGCATGCTAACTAG	GGACATCTAAGGGCATCACAG	37062833
CDKN1B	GCCCTCCCCAGTCTCTCTTA	CTCCCAAGCACCTCGGATTT	29311824
PPIA	GCCGAGGAAAACCGTGTACTA	TCTGCTGTCTTTGGGACCTT	29311824
RPL13A	GGTCCTGGTGCTTGATGGTC	GGCCCAGCAGTACCTGTTTA	21633896
RRP1	GAAACGCAGGGAGTGATGTG	GGATGCTGGCCCCTAATGAT	37062833
B2M	GATGAGTATGCCTGCCGTGT	GCGGCATCTTCAAACCTCCA	19818117
TBP	TGGCGTGTGAAGATAACCCA	GCAAACCAGAAACCCTTGCG	19818117
HPRT1	TTGCTTTCCTTGGTCAGGCA	ATCCAACACTTCGTGGGGTC	25289636

Table 6: Forward and reverse sequences of housekeeping genes in 5' to 3' that were screened including the literature source.

The CT values of all conditions 1) normoxia, 2) PBM, 3) hypoxia, and 4) hypoxia and PBM were grouped o identify the HK gene across all cell types with the lowest CT value range and standard deviation (Figure 4). There was only one stable HK gene throughout all four conditions in all cell types: *RPL13A*, encoding for the ribosomal protein L13a which catalyses protein synthesis.

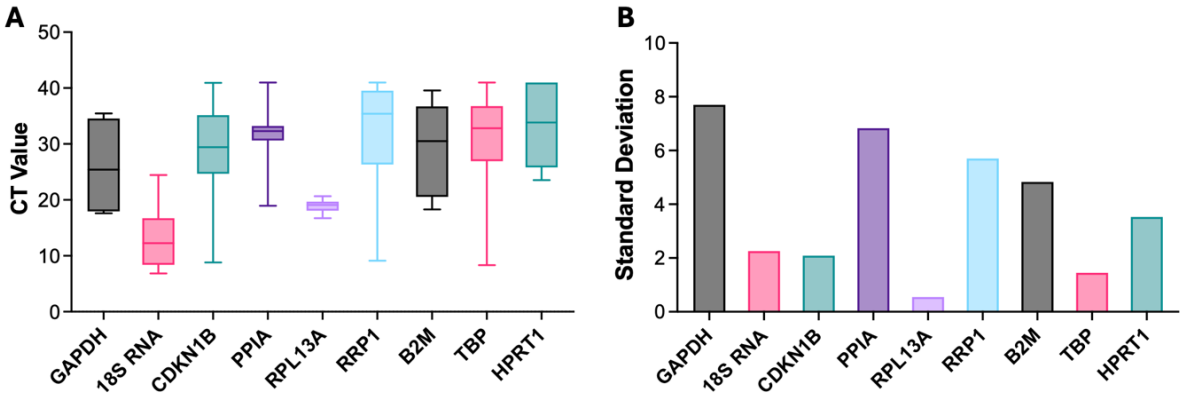


Figure 4: Identification of HK gene with the (A) CT values and (B) mean standard deviation (SD) for each gene. The highest variability was observed for GAPDH, PPIA, and RRP1, whereas the RPL13A had the lowest SD values.

3.9. Small interfering RNA transfection and knockdown

Small interfering RNA (siRNA) recognises and silences the target RNA and thus interferes with the translation to the protein. For one biological replicate treated with siRNA vWF (Life Technologies Ltd; AM16708), a 6-well plate was coated with Geltrex and $5x10^5$ HBMECs seeded per well. After two days of culture, cells were treated per well with siRNA as followed. 9 µL of Lipofectamine® RNAiMAX Reagent (Life Technologies Ltd; 13778-075) was diluted in 150 µL of Opti-MEM® Medium (Gibco; 31985062). Next, 3 µL of reconstituted and annealed siRNA for vWF (Working solution: 10 µM) was diluted in 150 µL of Opti-MEM® Medium. Both dilutions were then mixed 1:1 with 150 µL each and incubated at 25°C for 5 minutes. After the incubation, 250 µL siRNA-lipid complex was added to HBMECs. The cells were incubated at 37°C for 48 hours before lifting and pooling one 6-well plate as a biological replicate for further analysis. To confirm the knockdown of vWF, $5x10^5$ treated HBMECs were centrifuged and the pellet carefully washed with PBS. The pellet was resuspended in 350 µL of TRIzol to store at -20°C for subsequent qPCR analysis. To investigate the pathway involvement of vWF, four biological replicates of siRNA-treated HBMECs were cultured.

3.10. ROS-Glo™ H_2O_2 assay

ROS production was detected via the ROS-Glo™ H_2O_2 assay (Promega; G8820), following the manufactures protocol and using all reagents from the kit, and is a bioluminescent assay that measured the production of hydrogen peroxide (H_2O_2). HBMECs, HVPCs, and HAs were seeded in 96-well plates (1.5 x 10^5 cells) and cultured to a confluency of 80% (with 80 µL of media) before being exposed to the appropriate treatments. ROS levels were measured directly after normoxia or hypoxia as a baseline, after one, two, and three irradiations of PBM, and at 48 hours post-treatment for untreated and PBM-treated cells. The first step included the addition of 20 µL H_2O_2 Substrate Solution, mixed of 200 µL 10mM H_2O_2 Substrate and 2.5 µL 125 µM H_2O_2 Substrate Dilution Buffer calculated for 10 wells. Cells were incubated at 37°C for 1 hour in which the H_2O_2 substrate reacts with the produced H_2O_2 in cells to form the Luciferin precursor. Next the 100 µL supernatant was transferred to a white 96-well plate with clear bottoms for luminescence. The ROS-Glo™ detection solution was prepared immediately before use of 1 mL Luciferin Detection Reagent, 10 µL D-Cysteine, and 10 µL single enhancer solution for 10 wells. 100 µL of the ROS-Glo™ detection solution was added to the supernatant and incubated at 25°C for 20 minutes before measuring the luminescence using the CLARIOstar microplate reader. The RLU was calculated by dividing the luminescence of samples by the luminescence of their according cell-free media. The assay was measured in four biological replicates.

3.11. Seahorse real-time cell metabolic analysis

The mitochondrial function was based on the oxygen consumption rate (OCR) and the extracellular acidification rate (ECAR) measured via the Seahorse real-time cell metabolic analysis. HBMECs, HVPCs, and HAs were seeded on a Seahorse XF^e 96 cell culture plate (3.0 x 10^5 cells) (Agilent; 103794-100) with 2 biological replicates consisting of 10 technical replicates per cell type. The outermost wells were kept as a blank to normalise during the analysis. Cells were cultured for 2 days before being exposed to the appropriate treatment. The day prior to the analysis, the XF^e 96 FluxPak (Agilent; 102416-000) was rehydrated with 200 µL of the XF calibrant solution (Agilent; 100840-000) and kept in an incubator without CO_2 at 37°C overnight. The following day cells were washed twice with 50 µL of assay media, consisting of 40 mL of XF base medium (Agilent; 103575-100), 0.0728 g D glucose (10 mM) (Sigma-Aldrich; G7021), 0.00448 g sodium pyruvate (1 mM) (Sigma-Aldrich; P5280-25G), and 400 µL L-glutamine (2 mM) (Life Technologies; 25030024). Cells were then topped up with 175 µL of assay media and incubated without CO_2 at 37°C for 1 hour. To load the XFe96 FluxPak the following drugs were prepared in 3 mL of assay media: 1 µM Oligomycin (Working stock: 8 µM) (Sigma-Aldrich; O4876-5MG), 1 µM FCCP (Carbonyl cyanide-4 (trifluoromethoxy) phenylhydrazone) (Working stock: 9 µM) (Sigma-Aldrich; C2920-10MG), 0.5 µM Rotenone/Antimycin A (R/A) (Working stock: 5 µM) (Sigma-Aldrich: R8875-1G;A867a), and 50 mM 2-Deoxy-Glucose (2-DG) (Sigma-Aldrich; D8375-10MG). The XFe96 FluxPak was taken out of the incubator and 25 µL of the diluted Oligomycin added to port A, FCCP to port B, R/A to port C, and 2-DG to port D. The plate was placed back into the incubator and placed into the Seahorse XF^e 96 Extracellular Flux Analyzer (Agilent) to be calibrated when the cells had been incubating for around 40 minutes. After the pH and O_2 had been calibrated, the XF^e 96 cell culture plate was placed into the machine and the following measurements set per run: three for the baseline, five after Oligomycin treatment, three after FCCP injection, three after R/A injection, and 5 after the 2-DG treatment. Once the run was complete, the cells were dry frozen for

a subsequent protein quantification with the Pierce™ BCA protein assay kit (Thermo Scientific; 23225) following the manufacture protocol.

To quantify the protein concentration for each well, an albumin (BSA) standard dilution series was prepared ranging from 20 to 2,000 µg/mL. 30 µL of the standard series was added to the thawed cell plate with 30 µL dH_2O loaded to each cell. Next reagent A and B were mixed 50:1 with 200 µL being pipetted to each well and incubated at 37°C for 20 minutes. The absorbance was measured at 562 nm using the CLARIOstar microplate reader and the protein concentration calculated for each sample via the standard dilution series.

The OCR and ECAR measurements were then normalised to the protein concentration. The ATP production was calculated as the difference of basal respiration and the oligomycin injection. The proton leak was calculated as the measurements after oligomycin injection. The maximal respiration was calculated as the measurements after FCCP injection. The spare capacity was calculated as the difference between the maximal and basal respiration. The non-mitochondrial respiration was calculated as the measurements after R/A and subtracted from all OCR stages. The reserved glycolytic capacity was calculated as the difference of glycolytic ECAR and the oligomycin injection. The assays were measured in four biological replicates.

3.12. Proteome profiler human cytokine array

The Proteome Profiler Human Cytokine Array Kit (R&D Systems; ARY005B) is a membrane-based sandwich immunoassay and was used to detect 36 human cytokines, chemokines, and acute phase proteins in tri-cultures at 48 hours post-treatment. The assay was carried out following the manufacturers protocol with all reagents used from the kit. The membranes were blocked with the Array buffer 4 in a 4-well multi-dish for 25°C for 1 hours on a rocking shaker. Meanwhile the supernatant from all four groups was taken and any cell debris removed by centrifuging at 185 rcf for 2 minutes. The 1 mL of cell-free supernatant from each group was prepared in with 500 µL of Assay buffer 4. Then 15 µL of reconstituted Human Cytokine Array Detection Antibody Cocktail was added and the mixture incubated at 25°C for 1 hour. After aspirating the blocking solution, 1.5 mL of the incubated sample was pipetted to the membrane in the 4-well muti-dish and incubated at 4°C overnight. The following day, the membranes were washed three times in a petri dish of 20 mL of 1x Wash buffer. In the meantime, the Streptavidin-HRP was diluted 1:2000 in Array buffer 5 and 2 mL pipetted into each well of the 4-well multi-dish. The washed membranes were carefully placed into the multi-dish and incubated at 25°C for 30 minutes on a shaker. Next, membranes were washed three times with 1x Wash buffer and carefully places on the bottom sheet of a plastic sheet protector. Chemi Reagent 1 and 2 were mixed 1:1 and 1 mL pipetted onto each membrane. The top sheet of the plastic sheet protector was put on and air bubbles removed. After incubating for 1 minute, any excess Chemi Reagent mix was removed with absorbent wipes from the plastic sheet and the membranes. The top sheet was closed and membranes imaged with the iBright Imager 1500 (Invitrogen) auto-exposure system for 2:55 minutes and for 8:50 minutes, set by the smart range high dynamic range (HDR). The mean intensity for each dot was measured using Fiji Image J 1.54p and normalised to the mean intensity of the membrane background. The relative expression was calculated by normalising the mean intensity of each group to the untreated normoxia cells as the control. The measurements were taken in one biological replicate with two technical replicates.

3.13. Cell swelling assay

The swelling of astrocytes after hypoxia was assessed via live-cell calcein-AM imaging at 48 hours post-treatment by measuring the increase in area. The non-fluorescent and highly lipophilic compound calcein-AM easily diffuses into viable cells and becomes hydrolysed by the intracellular esterases into the fluorescent indicator calcein. Upon binding to intracellular Ca^{2+}, the calcein-Ca^{2+} complex emits a measurable green fluorescence light at 488 nm when excited, which is restricted to the area of the viable cell. Upon cell swelling, the cell's area increases which can be visualised via the intracellular calcein-Ca^{2+} complex. HAs (5.8 x 10^5 cells) were seeded on a PLL-coated (2µg/cm^2) coverslip (25mm in diameter) placed in a 6-well plate and exposed to the following conditions the following day: remained untreated in normoxia (control group), untreated after hypoxia, and PBM-treated after hypoxia. After 48 hours, the media was aspirated and exchanged with 1.5mL of calcein staining solution per coverslip, freshly prepared from 1.5mL PBS, 1µL calcein (1ug/ul) (Invitrogen; C1430), 2 drops NucBlue™ LiveReadyProbes™ Reagent (Invitrogen; R37605). Cells were incubated at 37°C for 20 minutes and washed with 3mL PBS. The coverslip was carefully placed in the live-cell imaging chamber and tightly sealed before pipetting 500 µL FluoroBrite ™ DMEM (Gibco; A1896701). Per coverslips, ten images were blindly captured using the Leica Thunder Imager (Leica Microsystems) at 20X magnification and processed with the small volume computational clearing. For quantitative analysis, the average the area normalised to the DAPI cell count was taken from the ten representative images and measurements were taken in three biological replicates. Cells were analysed via Fiji Image J 1.54p with Java 21.0.7 (64-bit).

3.14. Statistics

The data was analysed and plotted using the GraphPad Prism version 10.0. The results were expressed as mean ± standard error of the mean (SEM) values with a minimum of three biological replicates. For experiments comparing two independent groups, the p-values were calculated using two-tailed unpaired t test under the assumption of equal standard deviation. When comparing more than two groups, differences were assessed using a one-way ANOVA with Tukey's multiple comparisons test. For analysis requiring multiple pairwise comparisons across conditions, multiple t-test were performed with Holm-Šídák's correction. Statistical significance was defined as *$p<0.05$, **$p<0.01$, ***$p<0.001$, and ****$p<0.0001$.

4. RESULTS

4.1. Functional effect of PBM on the BBB in health and disease

4.1.1. Coating optimisation

The first aim of this project was to develop a functional *in vitro* model of the BBB, for which it is vital to establish a confluent monolayer of ECs. Thus, the coating for HBMECs was optimised to accommodate for an optimal and physiologically relevant environment. The apical side was coated with either PLL, Matrigel (200µL), or Geltrex (200µL), for HBMEC monocultures and co-cultures with HAs. Cultures coated with Geltrex constantly showed the highest TEER, in HBMEC monocultures compared to the uncoated control group (**$p<0.01$) and in co-cultures compared to the PLL coating, exhibiting the lowest TEER (*$p<0.05$) (Figure 5B). Therefore, Geltrex was chosen as the most suitable coating for all following *in vitro* transwell cultures.

4.1.2. PBM restored the barrier function after hypoxia

Upon coating optimisation, the impact of PBM on the BBB function in normoxia and after hypoxia (6 hours at 1% O_2) was assessed by measuring the change in relative TEER at 24 and 48 hours post-treatment. Figure 5A illustrates the workflow including the timeline of seeding at D1 and D2, hypoxia exposure and PBM treatment on D8, and follow-up analysis. In normoxia, PBM did not significantly alter TEER measurements and did not increase the barrier function (Figure 5C). The hypoxia conditions were chosen based on existing literature of BBB transwell models (Hayashi, Nakao et al. 2004, Chaudary, Karner et al. 2020). Whether the chosen O_2 concentration and duration of hypoxia was suitable to injure the barrier sufficiently was confirmed by TEER measurements. 6 hours at 1% O_2 significantly reduced the TEER for all cultures (*$p<0.05$) and was chosen as an appropriate environment to induce oxidative stress and dysfunction (Figure 5D). When the models

were pre-exposed to hypoxia and instantly irradiated with red and infrared light, the TEER in HBMEC monocultures and tri-cultures significantly recovered at both 24 and 48 hours (*p<0.05) compared to hypoxic only cultures (Figure 5E & F). EDTA-treated tri-cultures acts as the negative control with EDTA degrading tight junctions. Here, the negative control showed a dramatic drop in TEER and the responsiveness of the BBB model. These findings support the hypothesis, that PBM exhibit a therapeutic effect on the BBB integrity following hypoxic injury. Meanwhile, it also highlights that HBMEC monocultures are responsive to PBM alone and do not require the support of HAs and HVPCs to restore barrier function.

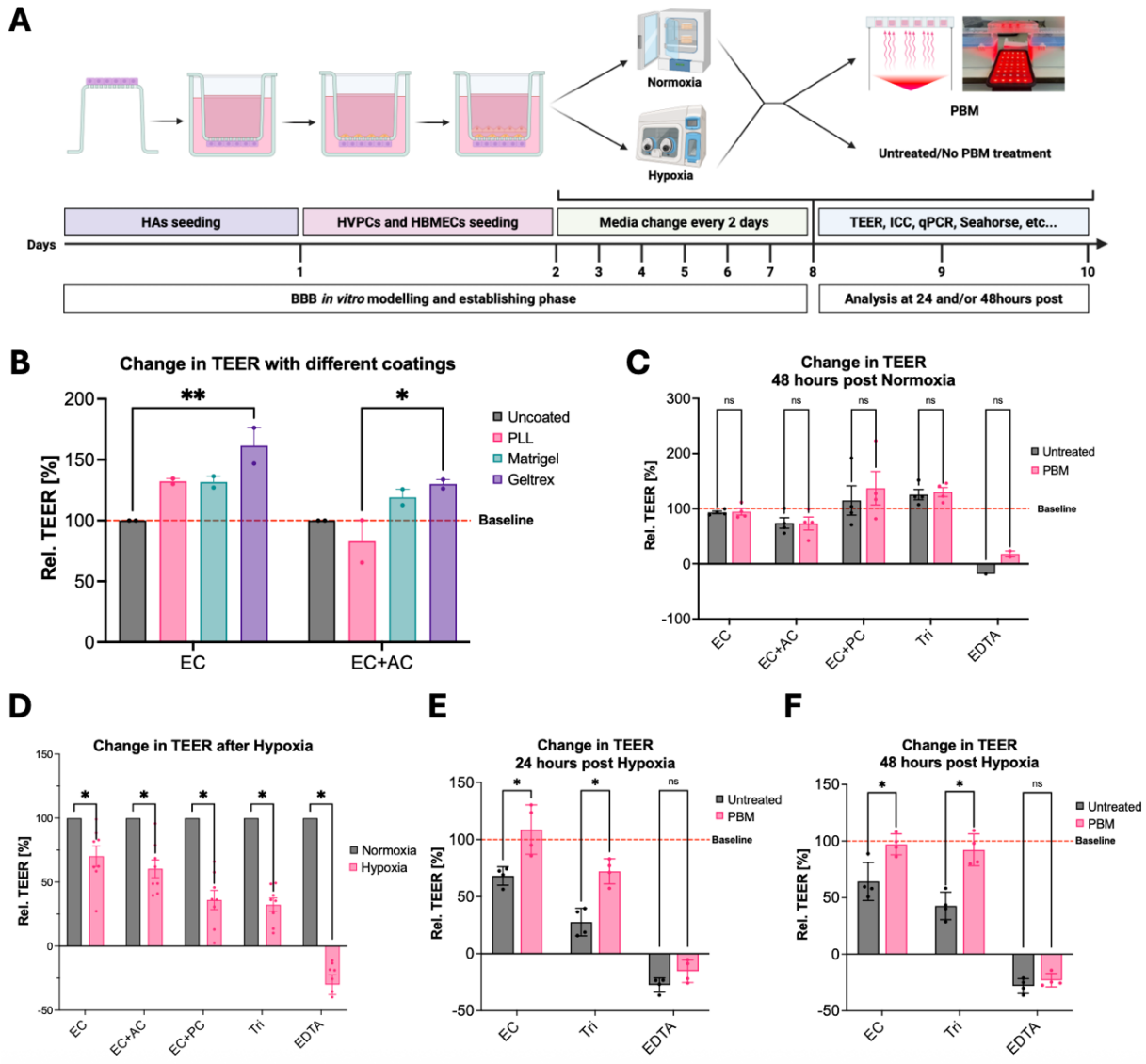


Figure 5: (A) Timeline of seeding the transwell model, exposure to groups, and follow-up analysis. Created with Biorender. (B) Quantification of the coating optimisation of the transwell model shown as the change of relative

*TEER for PLL, Matrigel, and GelTrex coating with the TEER normalised to the uncoated transwell. Two-way ANOVA (Tukey's multiple comparison test) with *p<0.05, **p<0.01 and n=2 (technical replicates). (C) Assessment of barrier function, shown as the change in relative TEER (%) at 48 hours post normoxia. (D) The impact of hypoxia (6 hours at 1% O_2) on the BBB function assessed by the drop in relative TEER. Assessment of barrier function at (E) 24 hours post hypoxia, and (F) 48 hours post hypoxia. Multiple unpaired t-test (Holm-Sidak methods) with *p<0.05 and N=4 (biological replicates). Error bars represent mean +/- SEM. EC: HBMEC monoculture; EC+AC: HBMEC/HA co-culture; EC+PC: HBMEC/HVPC co-culture; Tri: Tri-culture; EDTA: EDTA-treated tri-culture as negative control.*

4.1.3. Impact of PBM on tight junction expression

To understand whether the increase in TEER was driven by the upregulation of tight junction proteins and to double-validate the *in vitro* model, the expression of ZO-1 in HBMEC monocultures was analysed. Figure 6A-C shows the quantitative analysis in normoxia and Figure 6D-F in hypoxia. The levels of RNA expression of ZO-1 were normalised to the ZO-1 expression in untreated normoxic HBMECs. While PBM did not statistically upregulate ZO-1 on a genetic level in normoxia and hypoxia (Figure 6A & D), there seems to be a trend of increased expression compared to the non-PBM groups. ICC images (Figure 6C & F) clearly reflect the disruption of ZO-1 localisation after hypoxia with irregular and aberrant expression along the membranes. Quantification of the area of ZO-1 also revealed no difference between the untreated and PBM-treated groups in normoxia (Figure 6B) and hypoxia (Figure 6E). Nevertheless, PBM seems to improve ZO-1 localisation after hypoxia. Altogether, these results show that: 1) PBM does not impact the expression and localisation of ZO-1 in normoxia, 2) the improvement of barrier function with PBM after hypoxia is not driven by the upregulation or restoration of ZO-1, but by reorganisation and 3) the established *in vitro* model possesses a confluent HBMEC monolayer with consistent tight junctions.

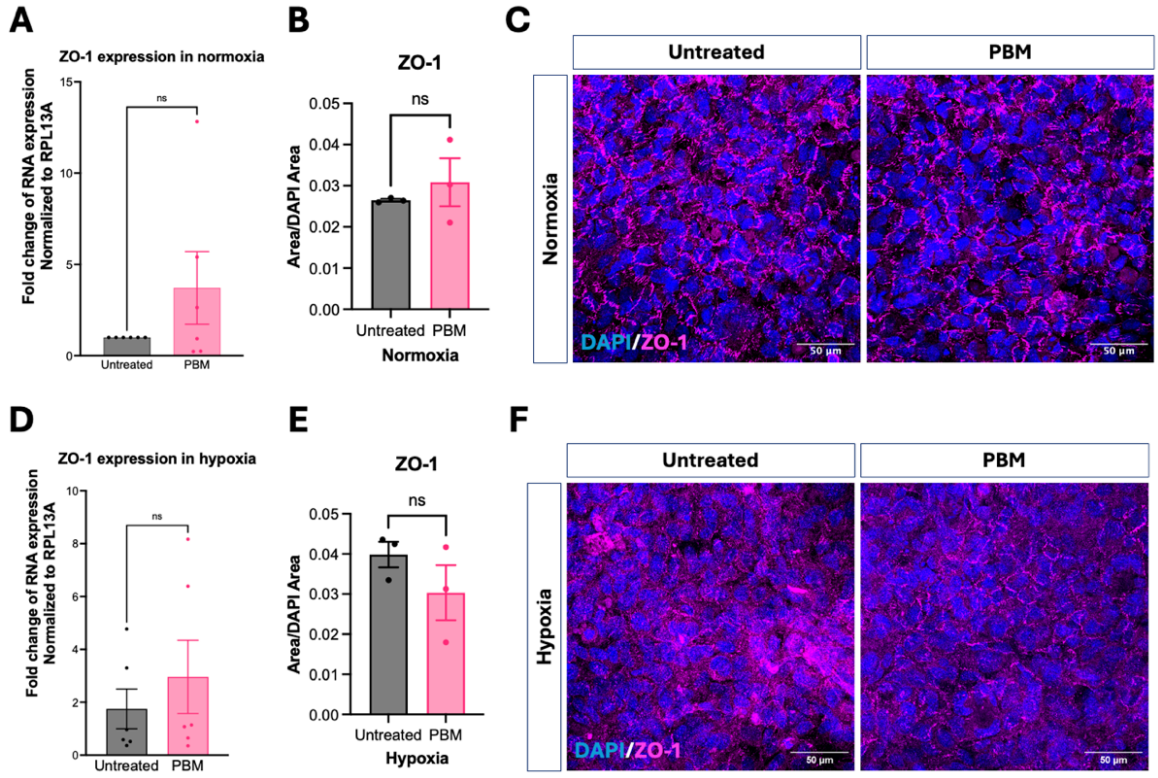


Figure 6: Expression of ZO-1 in (A-C) normoxia and (D-F) hypoxia. Fold change of ZO-1 RNA expression in (A) normoxia and (D) hypoxia groups. Quantification of ZO-1 protein expression from ICC, with the area of ZO-1 normalised to the area of DAPI, in (B) normoxia and (E) hypoxia groups. ICC images of ZO-1 (magenta) and DAPI (blue) in (C) normoxia and (F) hypoxia groups. Unpaired t-test with N=3-4 (biological replicates). Error bars represent mean +/- SEM.

4.1.4. Assessment of the cell viability, cytotoxicity, and apparent permeability

Since previous studies have reported that PBM can also boost cell viability in culture, the alamarBlue assay was carried out to assess cell viability of the transwell models. The fluorescence signal at 48 hours was taken relative to the baseline signal and showed, that PBM did not impact the cell viability of the mono- and tri-cultures in normoxia (Figure 7A) and after hypoxia (Figure 7B). Next, the ToxiLight cytotoxicity assay was carried out in cultures after hypoxia to investigate whether PBM reduces cell death. Findings on the relative luminescence show that PBM did not lower cell death after hypoxia compared to the non-PBM or untreated mono- and tri-cultures (Figure 7C). Taken together, these findings indicate that the noted increase in TEER for hypoxic cultures is

not due to an improved cell viability or diminished cell death. Therefore, there must be pathways which become activated by PBM after hypoxia that return the cell's behaviour into homeostasis and thus improve the barrier function. Moreover, the ToxiLight cytotoxicity assay revealed that PBM itself does not trigger cell death after hypoxia nor does it harm the cell's health.

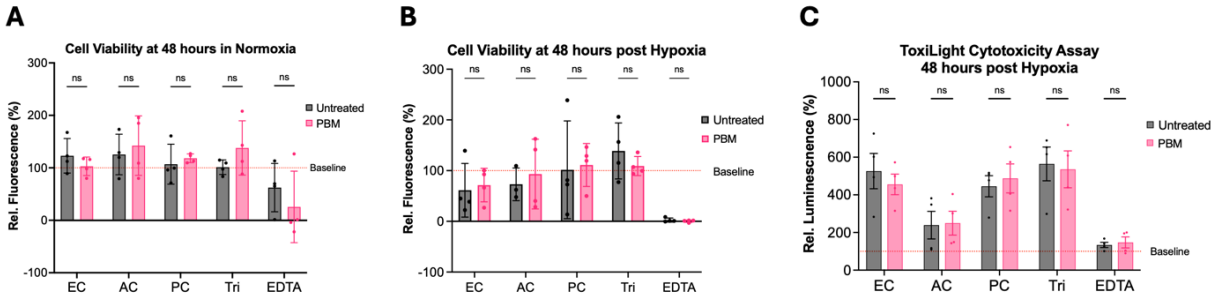


Figure 7: Quantification of the cell viability as the fluorescence signal (%) relative to the baseline signal after 48 hours for (A) normoxia and (B) hypoxia groups. (C) Quantification of the cytotoxicity as the relative luminescence signal (%) at 48 hours post hypoxia. Multiple unpaired t-test (Holm-Sidak methods) with N=4 (biological replicates). Error bars represent mean +/- SEM. EC: HBMEC monoculture; AC: HA monoculture; PC: HVPC monoculture; Tri: Tri-culture; EDTA: EDTA-treated tri-culture as negative control.

Moreover, the Papp calculated from the permeability assay using a fluorescence tracer, Alexa Fluor 488 10kDa, showed no significant changes in the diffusion over time of the tracer between non-PBM and PBM treated cultures in normoxia (Figure 8A) and hypoxia (Figure 8B). In a previous publication reported similar results where hypoxia (6 hours at 1% O_2) did statistically reduce the TEER of EC monocultures and co-cultured with PC but not in the permeability assay (Hayashi, Nakao et al. 2004).

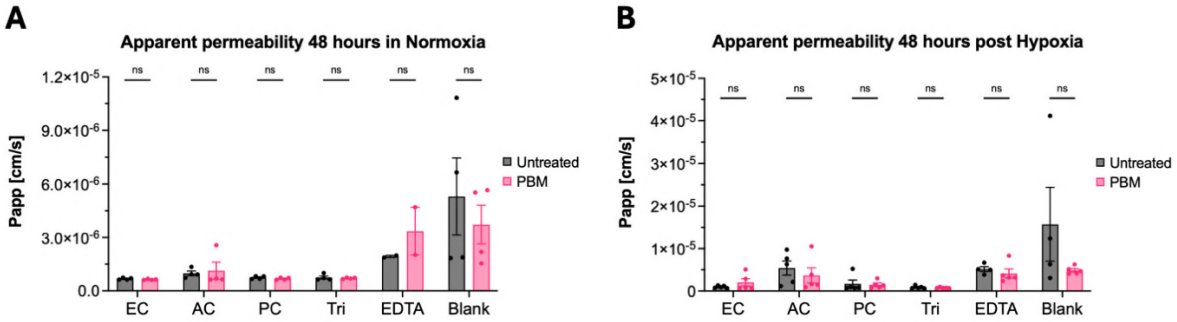


Figure 8: The apparent permeability (cm/s) at 48 hours in (A) normoxia and (B) hypoxia groups. Multiple unpaired t-test (Holm-Sidak methods) with N=4 (biological replicates). Error bars represent mean +/- SEM. EC:

HBMEC monoculture; AC: HA monoculture; PC: HVPC monoculture; Tri: Tri-culture; EDTA: EDTA-treated tri-culture as negative control.

4.2. Mitochondrial response to PBM

It is known that hypoxia impairs mitochondrial function and red and infrared light gets absorbed by the CCO, therefore whether PBM would alter the mitochondrial function in normoxia or hypoxia compared to non-PBM groups was tested next. To answer this question, the OCR and ECAR was measured using the Seahorse Real-Time Cell Metabolic Analysis for HBMECs, HAs, and HVPCs at 24 and 48 hours for all conditions. Cells were treated with 1) oligomycin, to inhibit Complex V of the ETC which reveals the ATP-linked OCR, 2) FCCP, an uncoupler that collapses the proton gradient and allows for maximal respiration, 3) R/A, to block Complex I and III essentially to shut down the mitochondrial respiration, and 4) 2-DG, an inhibitor of the hexokinase in the glycolysis pathway.

4.2.1. Analysis of the mitochondrial respiration

The OCR is a direct measure of consumed O_2 during oxidative phosphorylation, of mitochondrial respiration and how effectively energy is being produced. At 24 hours, hypoxia significantly reduced the basal respiration (pmol/min/µg protein) for HBMECs (***$p<0.001$) and HAs (*$p<0.05$), calculated as the average OCR before the injection of oligomycin (Figure 9B, F, & J). Interestingly, cells were able to recover to the control baseline level after 48 hours (Figure 9D, H, & L). To account for the change in basal respiration, the OCR (%) was first normalised to the protein concentration of each replicate and then taken relative to the basal respiration rates. Figures 9A, E, and I visualise the OCR over time after 24 hours, with hypoxic cells clearly showing an inconsistent and aberrant pattern of O_2 consumption compared to the control groups. This trend seems to normalise slightly after 48 hours as shown in Figure 9C, G, and K. Based on the OCR, the function and integrity of the mitochondria can be calculated as the fold change in ATP-linked respiration,

proton leak, maximal respiration, and spare capacity. Across all OCR analyses at 24 and 48 hours, there was no significant or relevant change observed between the normoxia groups.

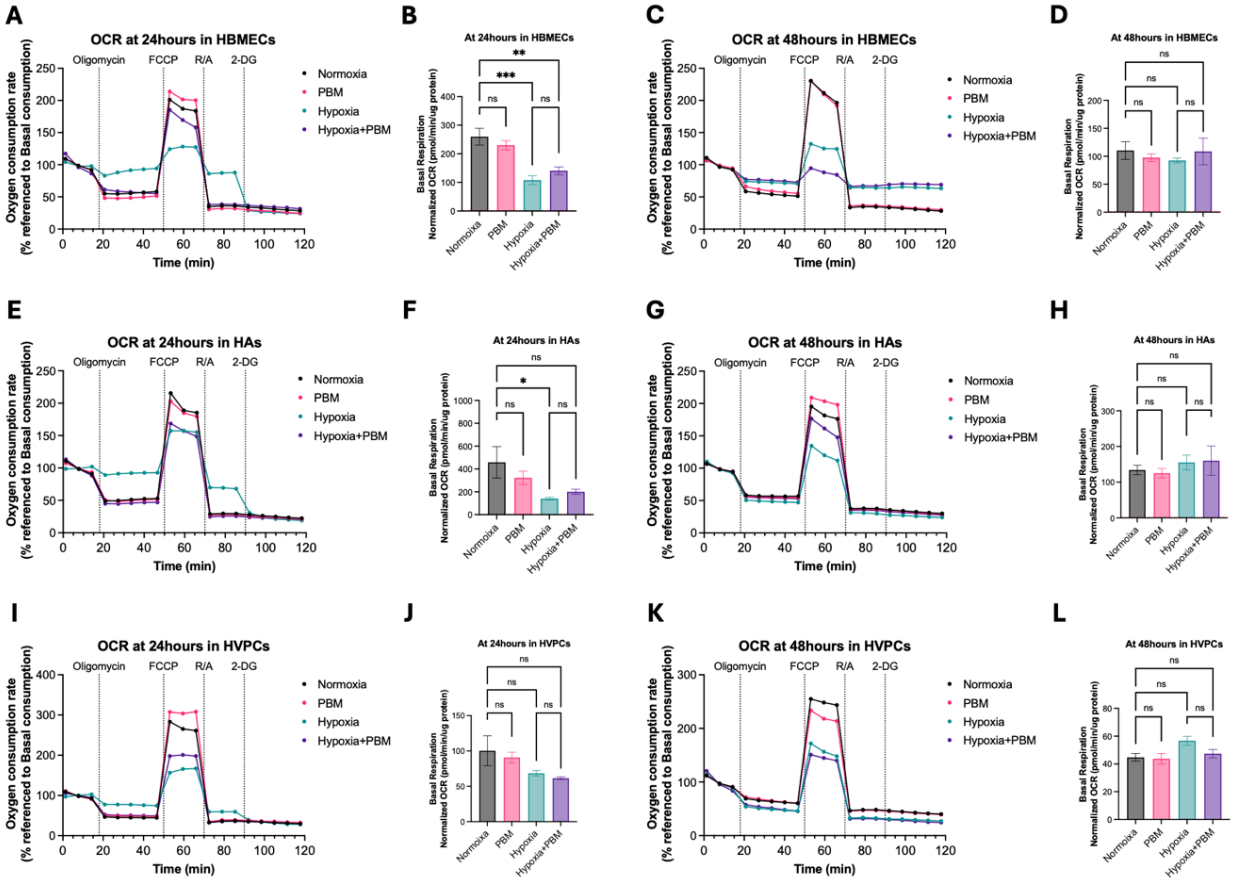


*Figure 9: Assessment of the OCR in HBMECs, HAs, and HVPCs at 24 hours (A, E, I) and at 48 hours (C, G, K) respectively. OCR (%) was normalised to protein concentration and to the basal OCR for all four conditions. The basal respiration (pmol/min/µg protein) was calculated before oligomycin injection for all conditions in HBMECs, HAs, and HVPCs at 24 hours (B, F, J) and at 48 hours (D, H, L) respectively. One-way ANOVA (Tukey's multiple comparisons test) with *p<0.05, **p<0.01, ***p<0.001 and N=4 (biological replicates). Error bars represent mean +/- SEM.*

At 24 hours, hypoxia strongly impairs the ATP-linked respiration in HBMECs (Figure 10A) which was almost restored back to the baseline after PBM, though not statistically significant (p=0.0758). This seemed to be a trend among the HAs and HVPCs as well (Figure 10E & I). Furthermore, PBM did significantly boost the maximal respiration of HBMECs after hypoxia compared to non-PBM hypoxic HBMECs (*p<0.05) (Figure 10C). HAs and HVPCs did not respond in a likewise manner and showed no difference within the hypoxia groups in their maximal respiration or spare capacity

(Figure 10G, H, K, & L). Surprisingly, the proton leak did not change at 24 hours for all cell types after hypoxia (Figure 10B, F, & J).

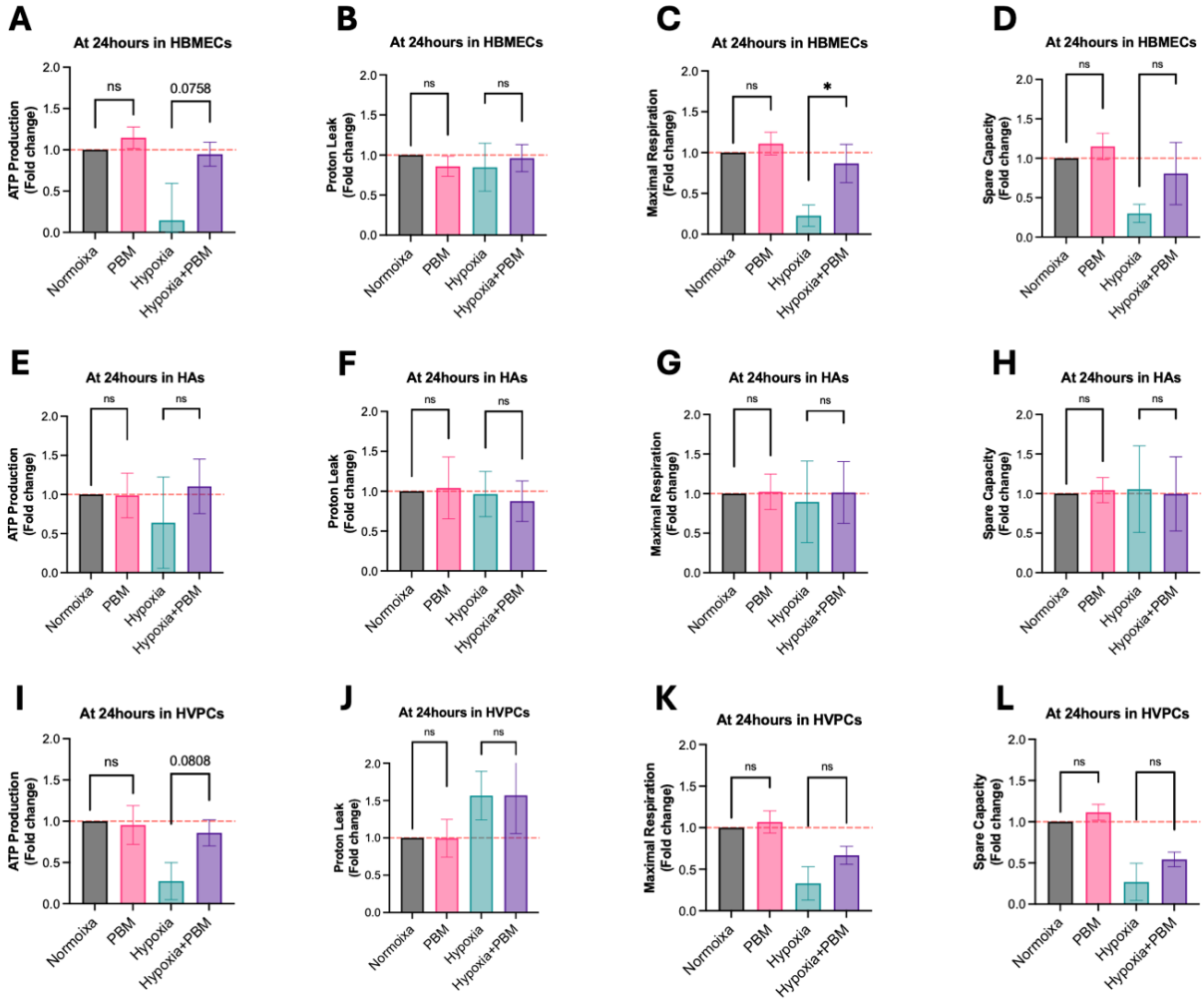


*Figure 10: Quantification of the fold change of the (A, E, I) ATP production, (B, F, J) proton leak, (C, G, K) maximal respiration, and (D, H, L) spare capacity at 24 hours, after normalisation to % of the basal OCR respiration, in (A-D) HBMECs, (E-H) HAs, and (I-L) HVPCs. The ATP production was calculated as the difference of basal respiration and the oligomycin injection. The proton leak was calculated as the measurements after oligomycin injection. The maximal respiration was calculated as the measurements after FCCP injection. The spare capacity was calculated as the difference between the maximal and basal respiration. The non-mitochondrial respiration was calculated as the measurements after R/A and subtracted from all OCR stages. One-way ANOVA (Tukey's multiple comparisons test) with *p<0.05 and N=4 (biological replicates). Error bars represent mean +/- SEM.*

As expected from the OCR plots, the four stages normalised after 48 hours in the hypoxia groups across the cell types seen in Figure 11. Overall, the hypoxia groups in HBMECs, HAs, and HVPCs showed a recovery of ATP-linked respiration (Figure 11A, E, & I). The proton leak was unchanged

for HAs and HVPCs and even decreased in HBMECs (Figure 11B, F, & J) below the normoxia values. Despite that, maximal respiration and spare capacity remained low in hypoxic HBMECs and dropped more in PBM treated hypoxic HBMECs, though not statistically different (Figure 11C & D). The maximal respiration and spare capacity in hypoxic HAs (Figure 11G & H) and HVPCs (Figure 11K & L) after 48 hours showed no statistical difference between PBM-treated and non-PBM groups and remained relatively similar to Figure 10. Surprisingly, PBM boosted the maximal respiration of HAs in normoxia (*$p<0.05$), an effect that seemingly improved the ATP production and spare capacity in HAs at 48 hours.

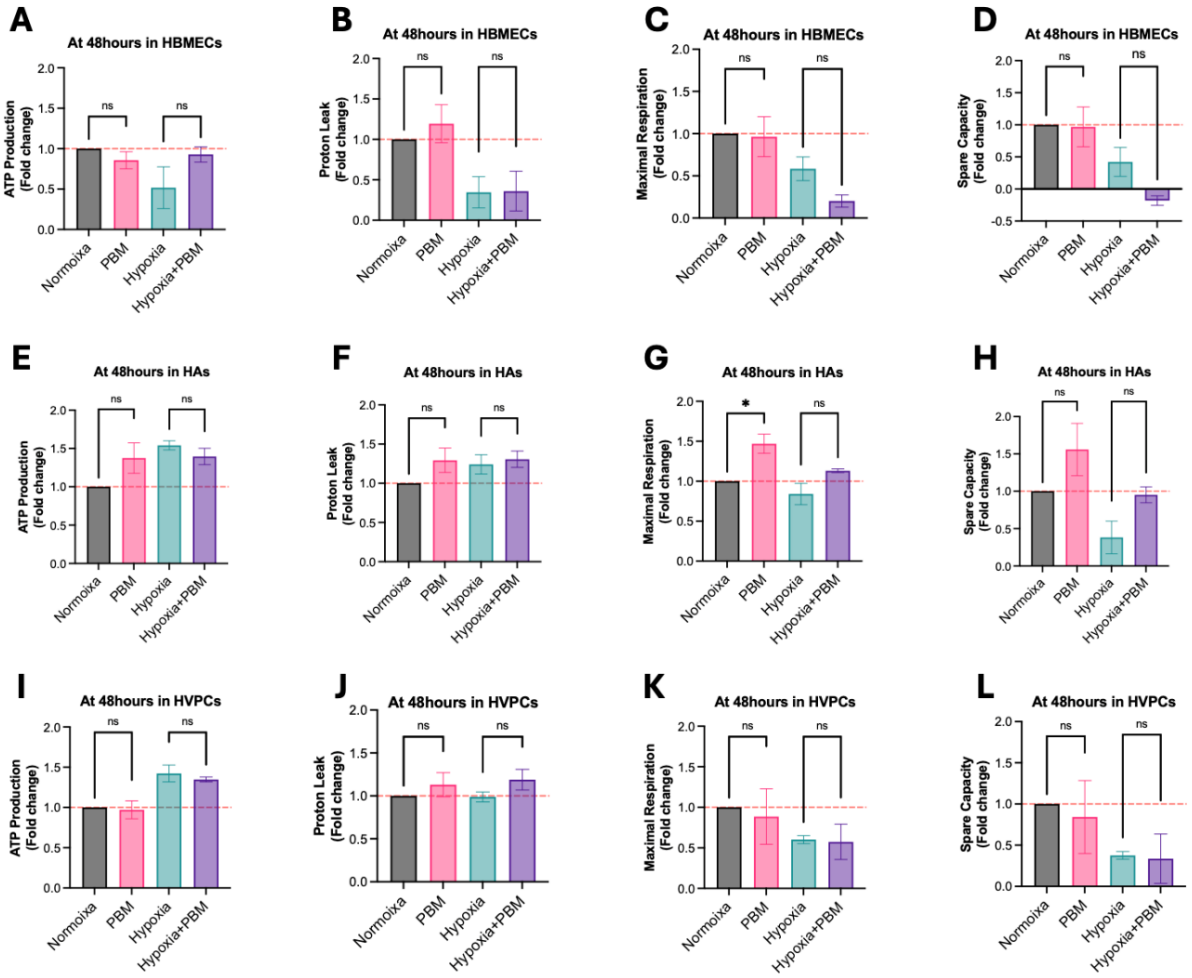


Figure 11: Quantification of the fold change of the (A, E, I) ATP production, (B, F, J) proton leak, (C, G, K) maximal respiration, and (D, H, L) spare capacity at 48 hours, after normalisation to % of the basal OCR respiration, in (A-D) HBMECs, (E-H) HAs, and (I-L) HVPCs. The ATP production was calculated as the difference of basal respiration and the oligomycin injection. The proton leak was calculated as the measurements after oligomycin injection. The maximal respiration was calculated as the measurements after FCCP injection. The spare capacity

*was calculated as the difference between the maximal and basal respiration. The non-mitochondrial respiration was calculated as the measurements after R/A and subtracted from all OCR stages. One-way ANOVA (Tukey's multiple comparisons test) with *p<0.05 and N=4 (biological replicates). Error bars represent mean +/- SEM.*

Taken together these findings show, that hypoxia impacts the basal respiration of HBMECs and HAs 24 hours after hypoxia which restored itself after 48 hours. While hypoxia impairs ATP production and maximal respiration in HBMECs, PBM significantly improved maximal respiration and to an extent the ATP-linked respiration. At 24 hours, HAs seem unaffected by hypoxia at various mitochondrial stages and PBM did not improve function in hypoxic HVPCs. Likewise, PBM did not enhance mitochondrial function at 48 hours post hypoxia as most levels normalised independently.

4.2.2. Analysis of the glycolytic respiration

The ECAR is a measure of protons which are released by cells and thus creating an acidic environment, primarily through glycolysis. Thereby, it reflects the cell's energy pathway and whether glycolysis is activated instead of oxidative phosphorylation. The basal ECAR (mpH/min/µg protein) was calculated as the average ECAR before oligomycin injection for all cell types and reflects the rate of glycolysis. Hypoxia did not affect the level of glycolysis at 24 hours (Figure 12A, E, & I) in HBMECs, HAs, and HVPCs. At 48 hours (Figure 12C, G, & K), glycolysis in hypoxic cells significantly dropped below the control for HBMECs (**p<0.01) and HVPCs (*p<0.05), as cells have mostly recovered from hypoxia. The reserved glycolytic capacity, represented as the fold change, was calculated from the rise in the ECAR after the oligomycin injection from the basal ECAR. PBM did not significantly affect or restore the reserved glycolytic capacity across all cell types at 24 hours (Figure 12B, F, & J) and 48 hours (Figure 12D, H, & L). In general, hypoxia reduced the glycolytic capacity in HBMECs and HAs at 24 hours which then restored in HAs at 48 hours. The glycolytic activity of HVPCs seemed to be mostly unaffected by hypoxia and PBM. Combining the findings from the ECAR and OCR analysis, it seems that cells utilise more energy from glycolysis at 24 hours after hypoxia since their basal OCR dropped but the glycolytic rate

remained stable. At 48 hours, the ECAR then decreases once the mitochondrial function of hypoxic cells stabilises. Overall, PBM did not affect the ECAR of HBMECs, HAs, and HVPCs in normoxia or hypoxia.

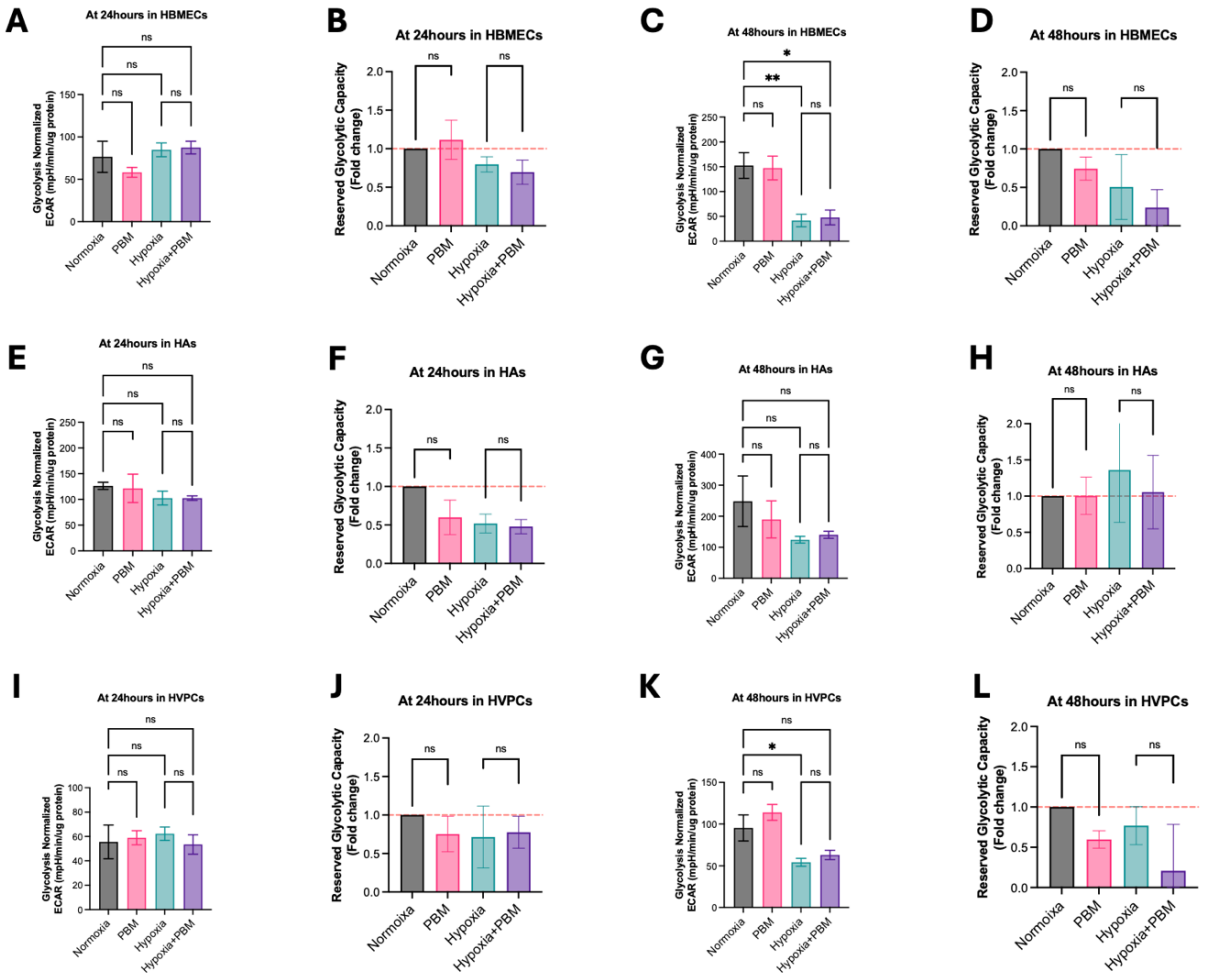


*Figure 12: The glycolytic ECAR (mpH/min/µg protein) was calculated as a measurement before oligomycin injection for all four conditions in HBMECs, HAs, and HVPCs at 24 hours (A, E, I) and at 48 hours (C, G, K) respectively. Quantification of the fold change of the reserved glycolytic capacity at (B, F, J) at 24 hours and (D, H, L) at 48 hours respectively. The reserved glycolytic capacity was calculated as the difference of glycolytic ECAR and the oligomycin injection. One-way ANOVA (Tukey's multiple comparisons test) with *p<0.05, **p<0.01 and N=4 (biological replicates). Error bars represent mean +/- SEM.*

4.3. PBM reduces oxidative stress

4.3.1. Downregulation of ROS upon PBM

Following the investigation of PBM on the mitochondrial function and based on previous findings that PBM can modulate ROS levels, changes in ROS production in normoxia and hypoxia were assessed next. Levels of ROS were measured at a baseline level and after one, two, and three rounds of light irradiation for each cell type. Moreover, to understand whether PBM impacts the synthesis of ROS long-term, measurements were also taken at 48 hours post-treatment. In normoxia, PBM did not statistically alter ROS levels, nor did it impact them after 48 hours compared to the control groups (Figure 13A-C). Similarly, PBM did not affect ROS levels in hypoxic HBMECs at any stage or after 48 hours (Figure 13D). The mitochondria of HBMECs were most affected by the induced oxidative stress, as observed from the OCR data, and maximal respiration was favoured by PBM after hypoxia (Figure 10C). While this could have beneficial effects in boosting the cell's energy production, this effect also represents greater probability of electron leakage contributing to ROS synthesis. Interestingly, hypoxic HAs immediately responded with a significant reduction of ROS synthesis after only one round of PBM compared to the baseline levels (**$p<0.01$) (Figure 13E). The drop remained constant throughout all consecutive irradiations (**$p<0.01$). This phenomenon was also observed in hypoxic HVPCs after three rounds of PBM (*$p<0.05$) (Figure 13F). At 48 hours ROS levels of both groups in hypoxic HAs and HVPCs stabilised showing no significant difference. This is not surprising as the basal OCR rates for both cell types at 48 hours after hypoxic also returned to baseline levels (Figure 9H & L). Accordingly, their energy demand depends on oxidative phosphorylation which can facilitate ROS production in hypoxia. Collectively, this supports the idea that PBM can act in an antioxidant manner and therefore alleviate cellular stress. In the tri-culture model, decreasing ROS levels in HAs and HVPCs might be one of the pathways by how PBM restored the BBB function after hypoxia. The boost in their cellular health might has strengthened their function in supporting the HBMEC barrier which was shown by an increase in TEER.

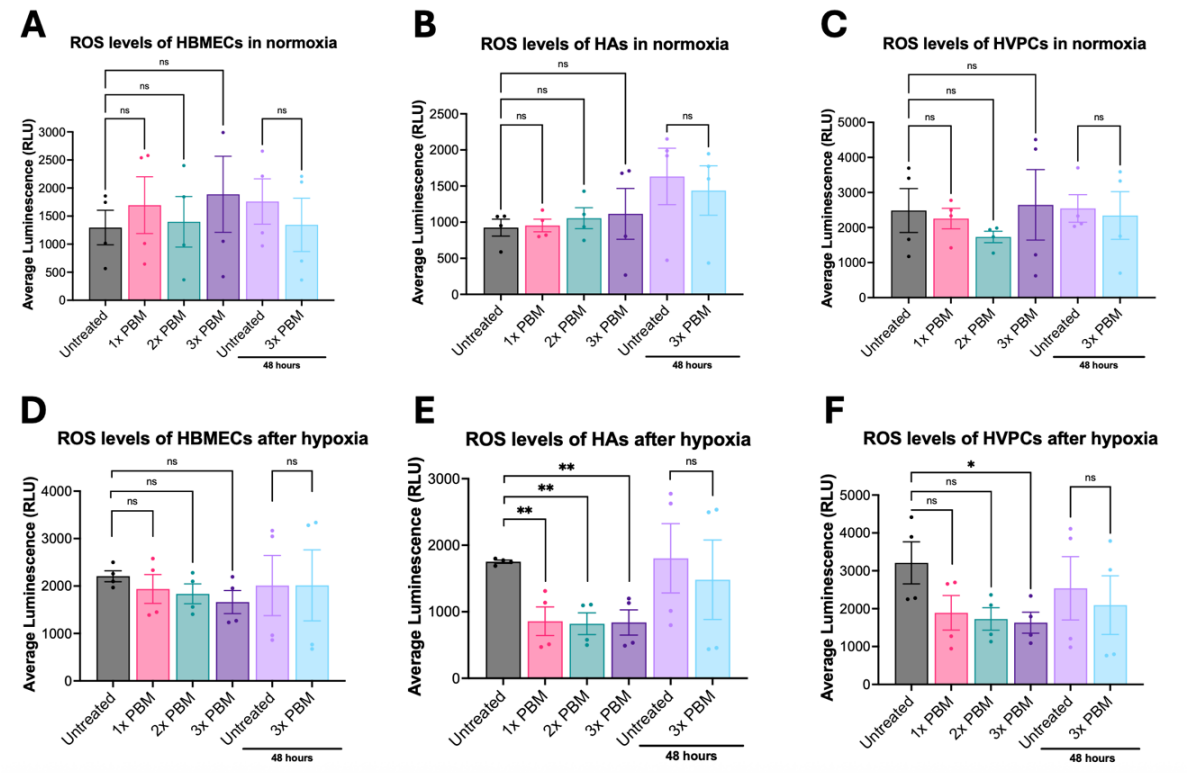


*Figure 13: Quantification of ROS levels in (A-C) normoxia and (D-F) hypoxia. (A-C) Average luminescence signal in (A) HBMECs, (B) HAs, and (C) HVPCs. (D-F) Average luminescence signal in (D) HBMECs, (E) HAs, and (F) HVPCs. One-way ANOVA (Tukey's multiple comparisons test) with *p<0.05, **p<0.01 and N=4 (biological replicates). Error bars represent mean +/- SEM.*

4.3.2. Dynamics of HIF-1α expression

To understand the downstream consequences of ROS modulation via PBM, the expression of HIF-1α, one of the key players during hypoxia, were examined. First, gene expression and ICC images were quantified at 48 hours of the monocultures post-treatment in normoxia. The protein expression of HIF-1α was calculated as the mean intensity co-localised with the cell nuclei (DAPI signal) since the factor localised to the nuclei to act as a transcriptional regulator in hypoxia. As shown in Figure 14C, F, & I, these levels remained low and did not change upon PBM exposure. In line with that, RNA expression of HIF-1α in HBMECs, HAs, and HVPCs treated with PBM showed no significant change to untreated normoxic cells (Figure 14A, D, & G). In normoxia, HIF-1α levels are not stabilised and marked for proteosome-mediated degradation. Accordingly, there was no

upregulation of HIF-1α observed. Next, the same quantitative analysis was conducted for HBMECs, HAs, and HVPCs at 48 hours post-treatment after hypoxia (Figure 15).

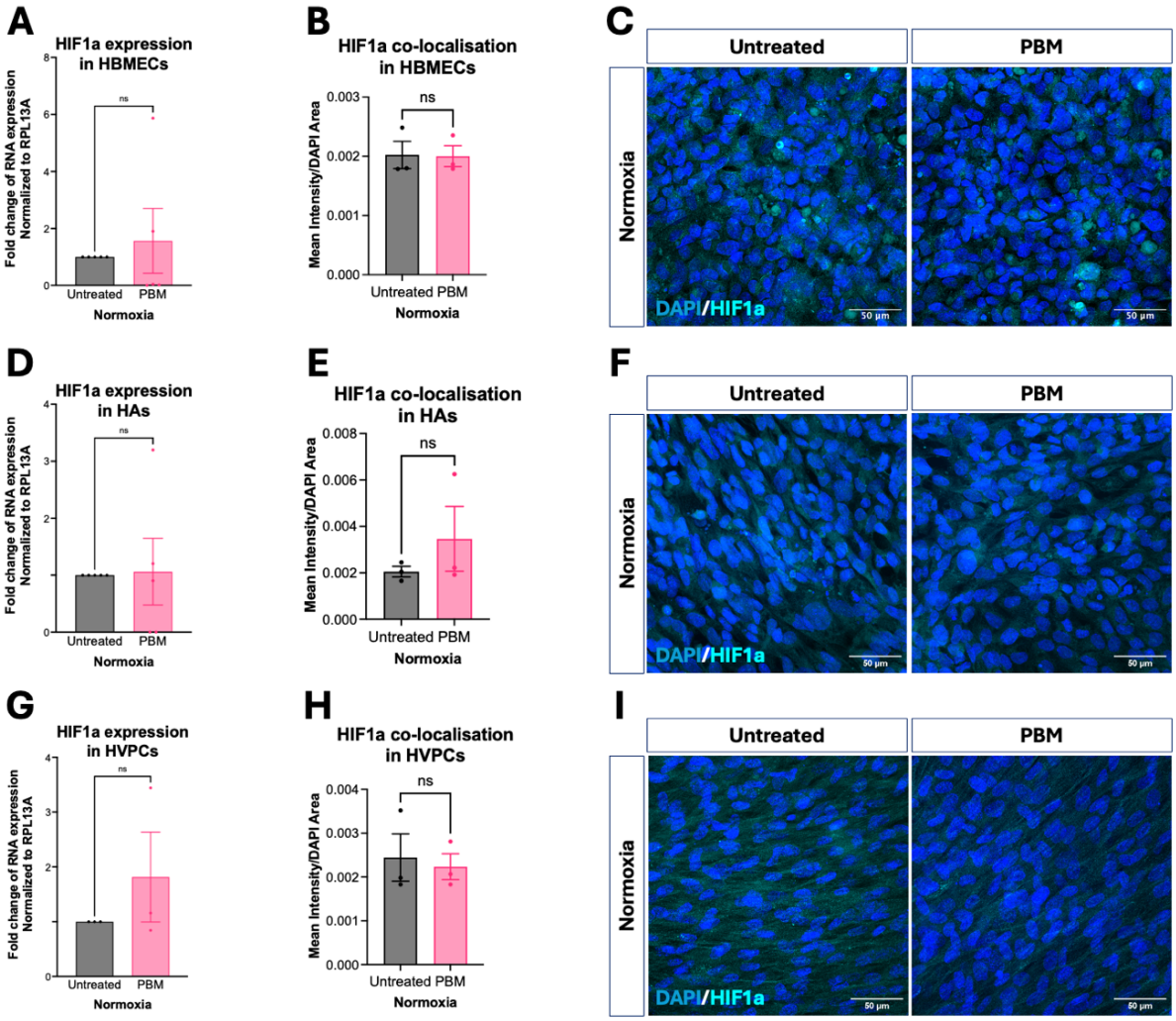


Figure 14: Expression of HIF-1α in normoxia in (A-C) HBMECs, (D-F) HAs, and (G-I) HVPCs. (A, D, G) Fold change of HIF-1α RNA expression in (A) HBMECs, (D) HAs, and (G) HVPCs. Quantification of HIF-1α protein expression, with the mean intensity normalised to the area of DAPI, in (B) HBMECs, (E) HAs, and (H) HVPCs. ICC images of HIF-1α (cyan) and DAPI (blue) in (C) HBMECs, (F) HAs, and (I) HVPCs. Unpaired t-test with N=3-4 (biological replicates). Error bars represent mean +/- SEM.

As expected, ICC revealed markedly increased HIF-1α expression within the nuclei and the cytoplasm after hypoxia for all cell types (Figure 15C, F, & I). Quantitative analysis of HIF-1α levels co-localised with DAPI, showed a significant reduction in HBMECs treated with PBM (*$p<0.05$) compared to hypoxic only cells (Figure 15B). This was backed up with the according RNA analysis which highlights a similar trend (Figure 15A). While PBM did not reduce ROS levels

in HBMECs after hypoxia, it did indeed statistically decrease HIF-1α levels. This downregulation could prevent damaging downstream events and boost cellular health. The expression patterns in HAs displayed a similar trend, yet neither the RNA expression (Figure 15D) or ICC analysis (Figure 15E) were statistically significant. In HVPCs, PBM did not modulate HIF-1α on a quantitative level (Figure 15G & H), still the distribution of HIF-1α in untreated groups seemed less organised than in PBM-treated hypoxic HVPCs.

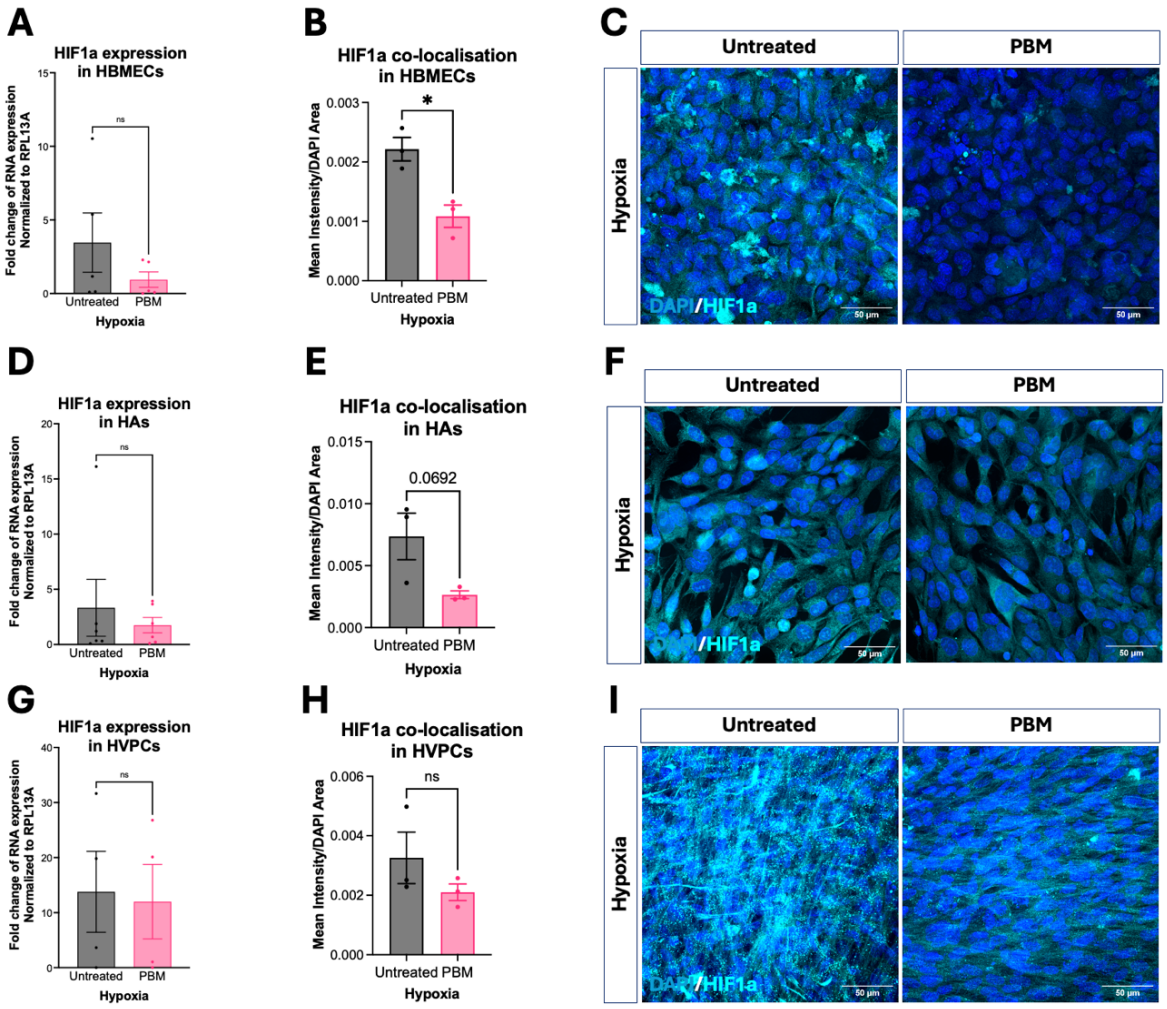


*Figure 15: Expression of HIF-1α post hypoxia in (A-C) HBMECs, (D-F) HAs, and (G-I) HVPCs. (A, D, G) Fold change of HIF-1α RNA expression in (A) HBMECs, (D) HAs, and (G) HVPCs. Quantification of HIF-1α protein expression, with the mean intensity normalised to the area of DAPI, in (B) HBMECs, (E) HAs, and (H) HVPCs. ICC images of HIF-1α (cyan) and DAPI (blue) in (C) HBMECs, (F) HAs, and (I) HVPCs. Unpaired t-test with *p<0.05 and N=3-4 (biological replicates). Error bars represent mean +/- SEM.*

4.4. PBM-mediated downregulation of vWF in HBMECs improves TEER

With PBM enhancing the TEER in HBMECs monocultures alone it hints that there is an independent pathway in HBMECs that responds to these wavelengths and rescues barrier function. In hypoxia, vWF and other platelet adhesion factors are released and damage the properties of the BBB. The qPCR data showed a significant upregulation in vWF RNA in non-PBM hypoxic HBMECs compared to untreated normoxic cells (****p<0.0001) (Figure 16A). This striking increase was also observed in vWF ICC staining of HBMECs at 48 hours (Figure 16C & E). Moreover, one of the most exciting findings was that PBM statistically downregulated RNA expression of vWF after hypoxia (****p<0.0001) (Figure 16A). This effect was found on a protein level with a significant reduction (*p<0.05) of the mean intensity of vWF in hypoxic HBMECs (Figure 16D). Given our understanding how vWF favours BBB permeability, these findings report a novel pathway to restore barrier function via downregulation of vWF using red and infrared light.

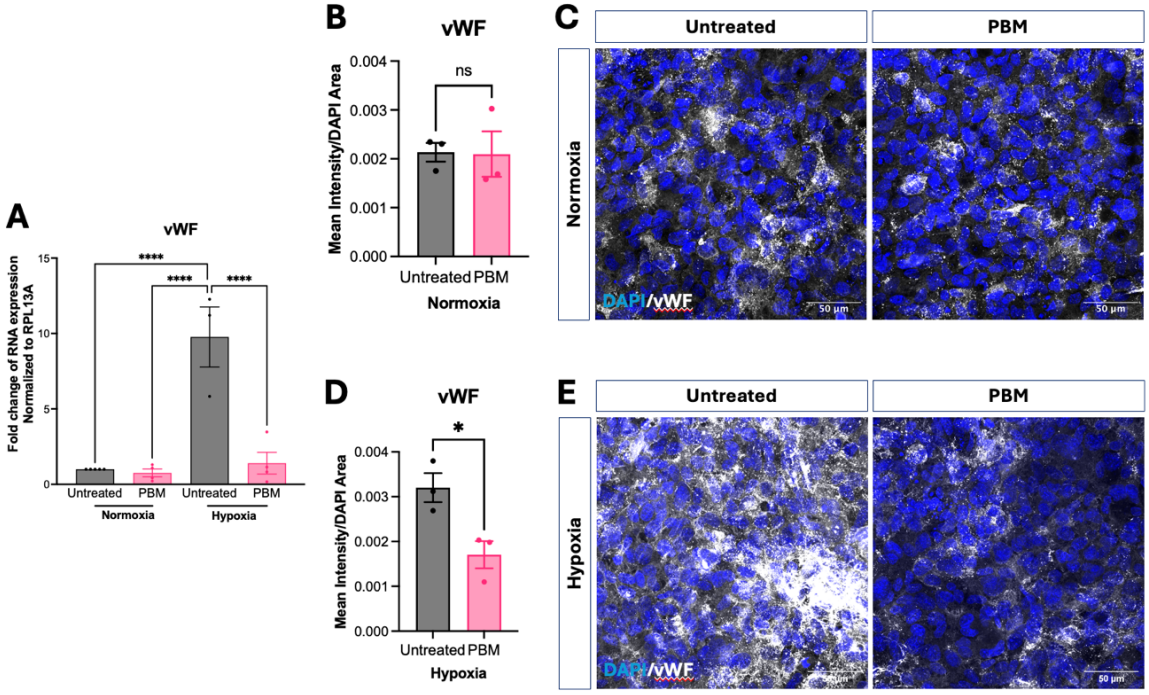


*Figure 16: Expression of vWF in (B-C) normoxia and (D-E) hypoxia. (A) Fold change of vWF RNA expression for all groups. One-way ANOVA (Tukey's multiple comparisons test) with ****p<0.0001 and N=3-4 (biological*

replicates). Quantification of vWF protein expression, with the mean intensity normalised to the area of DAPI, in (B) normoxia and (D) hypoxia groups. Unpaired t-test with N=3 (biological replicates). ICC images of ZO-1 (magenta) and DAPI (blue) in (C) normoxia and (E) hypoxia groups. Error bars represent mean +/- SEM.

4.4.1. siRNA depletion of vWF confirms its pathway involvement

To validate the involvement of vWF in improving the barrier function, HBMECs were transfected with siRNA targeting vWF via Lipofectamine™ RNAiMAX for an almost complete depletion of the corresponding RNA (****p<0.0001) (Figure 17A). After successful transfection, mono- and tri-cultures of vWF KO HBMECs for all four conditions were seeded. It was expected that there would be no difference in TEER between non-PBM and PBM-treated cultures, as vWF was depleted in all groups. Compared to untreated models, PBM did not increase the TEER of mono- or tri-cultures at 24 or 48 hours in normoxia (Figure 17B) and hypoxia (Figure 17C). Therefore, these findings must indicate that the downregulation of vWF upon PBM in hypoxic HBMECs, as observed in Figure 16, directly contributes to the improvement of barrier integrity manifesting with an increase in TEER.

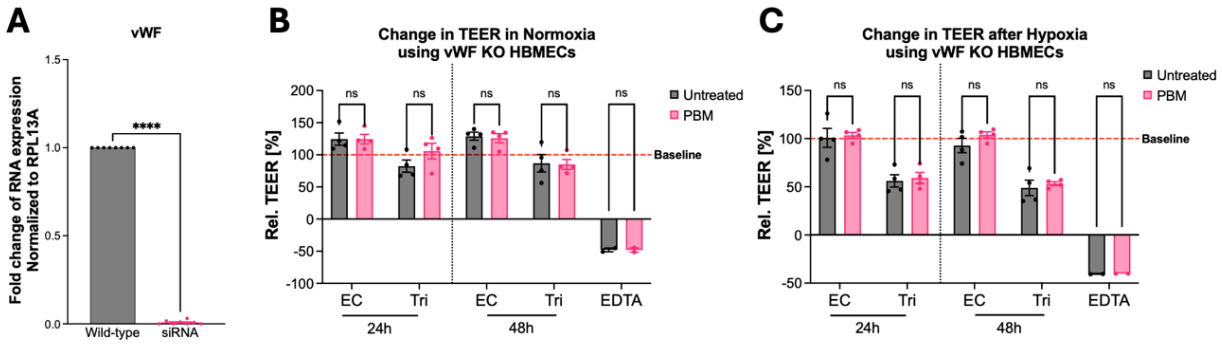


*Figure 17: (A) RNA expression of vWF in wild-type and siRNA-treated HBMECs. Unpaired t-test with ****p<0.0001 and N=8 (biological replicates). Assessment of barrier function, shown as the change in relative TEER (%) at 24 and 48 hours (B) in normoxia and (C) post hypoxia. Multiple unpaired t-test (Holm-Sidak methods) with N=4 (biological replicates). Error bars represent mean +/- SEM. EC: HBMEC monoculture; Tri: Tri-culture; EDTA: EDTA-treated tri-culture as negative control.*

4.5. PBM modulates cytokines and chemokines

Inflammatory pathways are active as an acute response to hypoxia. Therefore, whether PBM modulates such cytokine, chemokines, and acute phase proteins was tested next. To assess the protein expression of various markers simultaneously, the Proteome Profiler Human Cytokine Array detecting various human cytokines and more was chosen. The membranes were incubated with debris free supernatant collected from tri-cultures which were previously exposed to all conditions. Out of 17 detected cytokines, chemokines, and acute phase proteins, only six showed a statistical difference between the untreated and PBM-treated groups which are shown in the representative Figure 18. Interestingly, PBM already modulated levels in normoxia and led to a significant upregulation of chemokines Interleukin-8 (IL-8) (***$p<0.001$; Figure 18B) and growth-regulated oncogene-α (CXCL1/GROα) (***$p<0.001$, Figure 18E) and cytokines interleukin-21 (IL-21) (***$p<0.001$; Figure 18C), granulocyte-macrophage colony-stimulating factor (GM-CSF) (***$p<0.001$; Figure 18F), and migration inhibitory factor (MIF) (***$p<0.001$; Figure 18G) compared to the untreated group. In hypoxia, PBM also enhanced expression of IL-8 (*$p<0.05$; Figure 18B) and CXCL1/GROα (*$p<0.05$, Figure 18E) and cytokines IL-21(**$p<0.01$; Figure 18C) and GM-CSF (*$p<0.05$; Figure 18F), but less significant to normoxia. In contrast, SerpinE1/PAI-1, which is a pro-thrombotic marker released by ECs, was downregulated by PBM both in normoxia (***$p<0.001$) and hypoxia (*$p<0.05$) (Figure 18D). Taken together, the results indicate that PBM impacts the immune regulation and response, while reducing the overall blood clot formation in normoxia and after hypoxia. These changes could have protective effects and lead to the repair of the damaged BBB after oxidative stress.

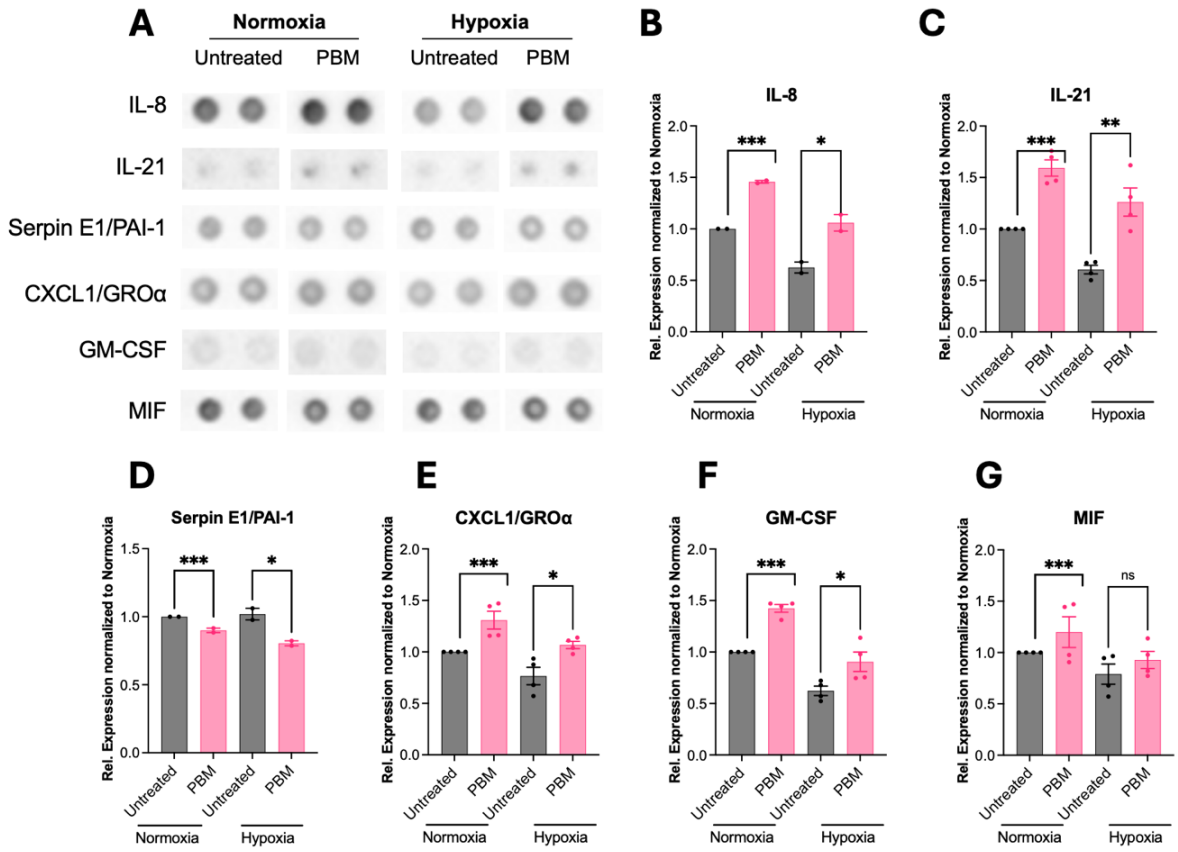


*Figure 18: (A) Representative image from the iBright imager of positive and significant markers from the Proteome Profiler Human Cytokine Array. The intensity of two dots per group was averaged and the background intensity subtracted. Relative expression levels were normalised to the untreated normoxia group of (B) IL-8, (C) IL-21, (D) Serpin E1/PAI-1, (E) CXCL/GROα, (F) GM-CSF, and (G) MIF. Unpaired t-test with *p<0.05, **p<0.01, ***p<0.001 and n=2 (technical replicates). Error bars represent mean +/- SEM.*

4.6. Impact of PBM on HAs

4.6.1. AQP4 dynamics

Perivascular ACs activate neuroinflammatory pathways and delocalise AQP4 in hypoxia which are known to weaken the BBB integrity. Following the insight that HAs responded to PBM with a drop in ROS levels, the AQP4 dynamics and cell swelling upon PBM in normoxia and hypoxia were investigated further. In normoxia and hypoxia, PBM did neither increase nor decrease the RNA expression of AQP4 in HAs monocultures (Figure 19A). The quantitative analysis of ICC images, staining for both the M1 and M23 AQP4 isoforms, showed similar results to the qPCR, with no significant difference between the groups (Figure 19B & D). Still, in the ICC of PBM-treated hypoxic HAs there was a trend towards a reduced expression of AQP4.

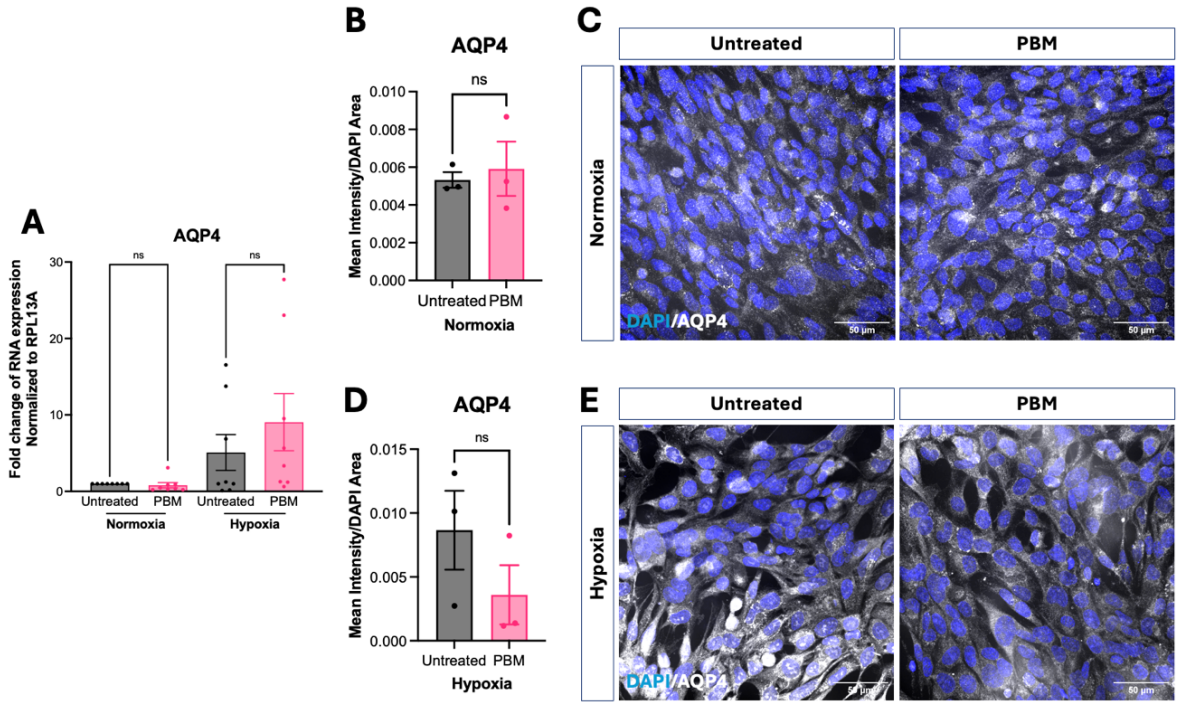


Figure 19: Expression of AQP4 in (B-C) normoxia and (D-E) hypoxia. (A) Fold change of AQP4 RNA expression for all groups. One-way ANOVA (Tukey's multiple comparisons test) with N=5 (biological replicates). Quantification of AQP4 protein expression, with the mean intensity normalised to the area of DAPI, in (B) normoxia and (D) hypoxia groups. Unpaired t-test with N=3 (biological replicates). ICC images of AQP4 (grey) and DAPI (blue) in (C) normoxia and (E) hypoxia groups. Error bars represent mean +/- SEM.

To further analyse whether this trend functionally affects the HAs in hypoxia, a live-cell calcein-AM imaging at 48 hours after hypoxia was conducted (Figure 20). While calcein-AM easily penetrates into the cell via passive diffusion, it's efflux via the ATP-binding cassette (ABC) transporter impacts the calcein retention and may be affected by prolonged oxygen levels which in turn impact the calcein staining (Ansbro, Shukla et al. 2013). It appeared that HAs started to swell after hypoxia and PBM reversed that effect. Yet, there was no statistical significance observed between the groups (Figure 20B). Summing up, PBM only displayed a slight trend in positively affecting AQP4 dynamics, localisation, or swelling of HAs.

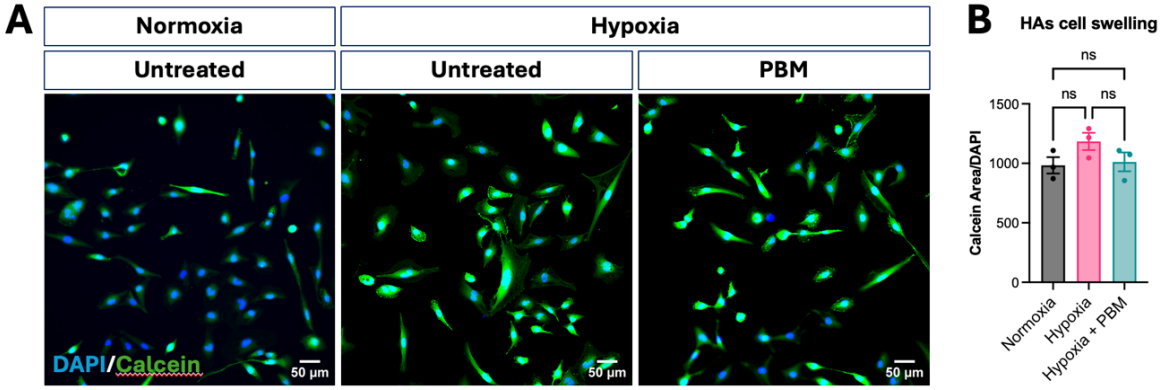


Figure 20: (A) Example of live-cell images to assess HAs cell swelling with calcein (green) and DAPI (blue) for hypoxia groups and the untreated normoxia group (control). (B) Quantification of cell swelling, with the mean area normalised to the DAPI cell count. One-way ANOVA (Tukey's multiple comparisons test) with N=3 (biological replicates). Error bars represent mean +/- SEM.

4.6.2. Expression of the glial fibrillary acidic protein

The glial fibrillary acidic protein (GFAP) is a key structural marker for ACs and upregulated during trauma, neuroinflammation, and hypoxia. Since ACs become reactive during hypoxia and play into inflammatory pathways, the GFAP upregulation and effect of PBM were investigated. RNA levels of GFAP from untreated HAs in normoxia and after hypoxia showed no significant upregulation. Likewise, there was no difference observed between the hypoxia only and hypoxia PBM-treated groups on gene expression (Figure 21A). HAs were stained at 48 hours for GFAP and the analysis

of the mean intensity revealed no effect of PBM on GFAP in normoxia or hypoxia (Figure 21B & D).

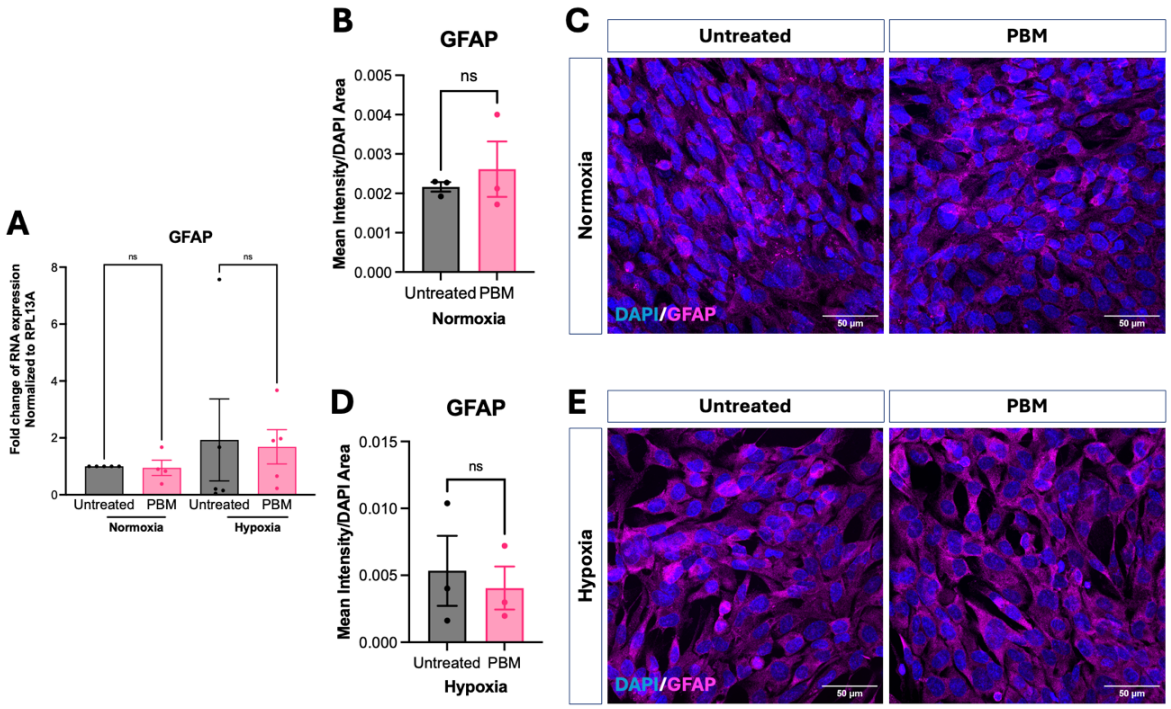


Figure 21: Expression of GFAP in (B-C) normoxia and (D-E) hypoxia. (A) Fold change of GFAP RNA expression for all groups. One-way ANOVA (Tukey's multiple comparisons test) with N=5 (biological replicates). Quantification of GFAP protein expression, with the mean intensity normalised to the area of DAPI, in (B) normoxia and (D) hypoxia groups. Unpaired t-test with N=3 (biological replicates). ICC images of GFAP (magenta) and DAPI (blue) in (C) normoxia and (E) hypoxia groups. Error bars represent mean +/- SEM.

4.7. Impact of PBM on HVPCs

4.7.1. Expression of PDGFRβ

Our understanding of PBM on HVPCs is limited and it is unknown how the expression of PDGFRβ changes and whether it might contribute to the TEER improvements. ICC images (Figure 22C & E) at 48 hours post treatment, clearly displayed a reduction of PDGFRβ after hypoxia with was characterised by a lower intensity and delocalisation. While the quantification of the mean intensity of PDGFRβ revealed a downregulation of around 50% between normoxia and hypoxia, there was no difference between the non-PBM and PBM-treated groups for both conditions (Figure 22B & D). Since the expression of PDGFRβ was too low to be detectable in hypoxic HVPCs, the RNA expression of Rgs5, an upstream regulator of PDGFRβ during hypoxia, was analysed (Figure 22A). Contradictory to the literature, Rgs5 is clearly downregulated in hypoxic HVPCs which would indicate that the loss of PDGFRβ is depended on other pathways during hypoxia. Overall, PBM did not alter the expression of PDGFRβ or Rgs5 in HVPCs during normoxia or hypoxia compared to untreated or non-PBM HVPCs.

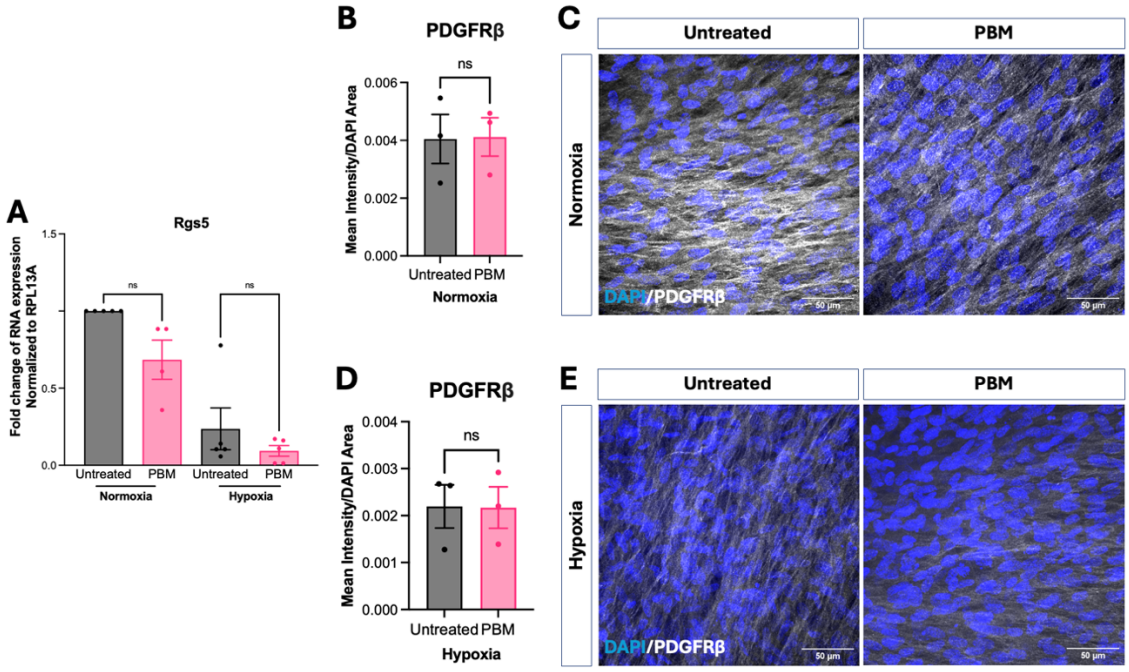


Figure 22: Expression of PDGFRβ in (B-C) normoxia and (D-E) hypoxia. (A) Fold change of Rgs5 RNA expression for all groups. One-way ANOVA (Tukey's multiple comparisons test) with N=5 (biological replicates).

Quantification of PDGFRβ protein expression, with the mean intensity normalised to the area of DAPI, in (B) normoxia and (D) hypoxia groups. Unpaired t-test with N=3 (biological replicates). ICC images of PDGFRβ (grey) and DAPI (blue) in (C) normoxia and (E) hypoxia groups. Error bars represent mean +/- SEM.

4.7.2. Dynamics of actin upon PBM

Lastly, to understand the changes in actin organisation and αSMA dynamics, their expression in HVPCs, as they can regulate the cerebral blood flow, were further investigated. Interestingly, the RNA expression of αSMA normalised to the untreated normoxia group, revealed no statistical changes within and between the groups (Figure 23A). Indeed, commonly observed vasoconstriction during hypoxia or ischemia could be a consequence of upregulated ROS levels rather than αSMA in PCs. Quantification of the mean intensity of actin from the ICC images at 48 hours post treatment, stained with an actin binding dye, showed no difference between the non-PBM and PBM-treated groups for normoxia (Figure 23B) and hypoxia (Figure 23D). Nonetheless, the organisation of actin in hypoxic HVPCs seems to be altered from PBM with less polymerisation and finer filaments (Figure 23E). Still, PBM did not alter the expression of αSMA or actin in HVPCs during normoxia or hypoxia compared to non-PBM HVPCs.

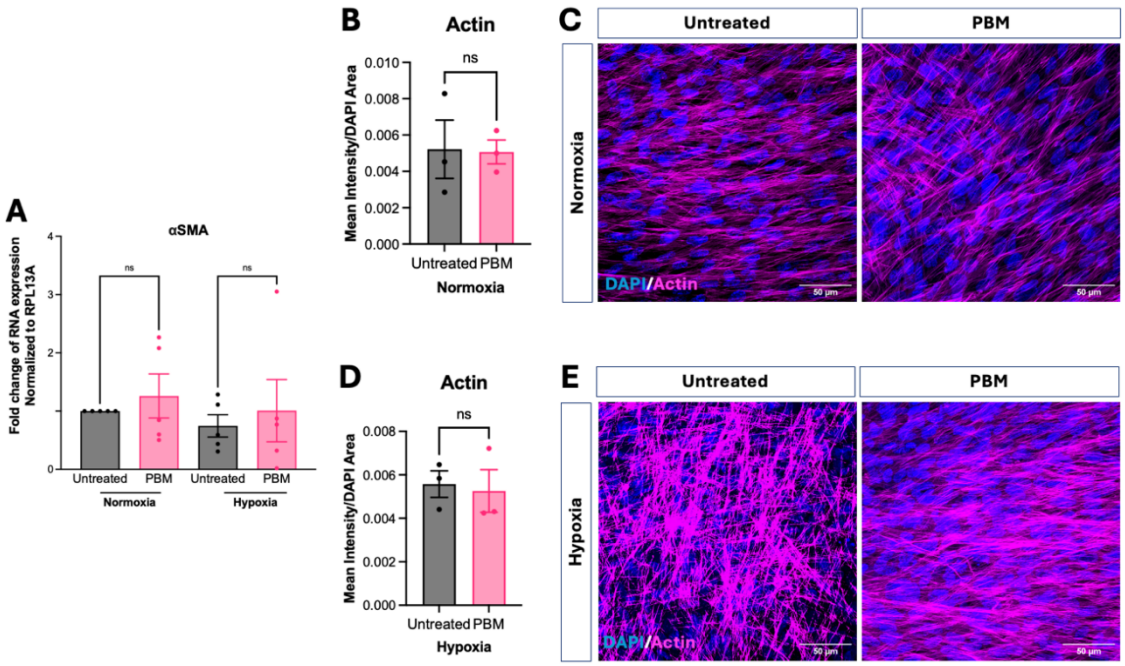


Figure 23: Expression of Actin in (B-C) normoxia and (D-E) hypoxia. (A) Fold change of αSMA RNA expression for all groups. One-way ANOVA (Tukey's multiple comparisons test) with N=5 (biological replicates).

Quantification of Actin protein expression, with the mean intensity normalised to the area of DAPI, in (B) normoxia and (D) hypoxia groups. Unpaired t-test with N=3 (biological replicates). ICC images of Actin (magenta) and DAPI (blue) in (C) normoxia and (E) hypoxia groups. Error bars represent mean +/- SEM.

5. DISCUSSION

PBM is a non-invasive red and infrared light therapy with broad therapeutic effect that have been previously shown for wound healing, Alzheimer's disease, and ischemic stroke. One of the key, but often overlooked player in brain health is the BBB. Impairment of the BBB is associated with almost all neurological and neurodegenerative diseases, and it is highly relevant to find strategies that restore BBB dysfunction. The aim of this study was to understand whether PBM improves the BBB function in health and disease and decipher the associated cell-specific molecular mechanisms. My findings suggest that only three sessions of 5-minute PBM irradiation is enough to repair the BBB integrity and return aberrant pathways to homeostasis after a hypoxic insult, supporting the idea that PBM is a therapeutic strategy against BBB dysfunction in disease.

For this study the transwell system was used to model the BBB *in vitro* and to investigate cell-specific effects, a novel method which is currently underrepresented in publications on PBM. Even though it is a gold standard model in research, the TEER measurements strongly vary between publications. Next to the transwell size and pore size, and type of culture e.g., contact or non-contact culture, the cultured cell type significantly impacts TEER values. A review comparing various models reported a TEER of 100 – 300 $\Omega \cdot cm^2$ for mouse primary EC monocultures while measuring a TEER of 250 $\Omega \cdot cm^2$ in hPSC-derived brain EC monolayers rising up to 1450 $\Omega \cdot cm^2$ when co-cultured with rat ACs (Helms, Abbott et al. 2016). In this study, commercially available immortalised human cell lines were used, as they produce a consistent TEER with low variability across replicates, are affordable, and proliferate at a high rate leaving a higher cell count compared to primary human cell lines. Stable cell lines exhibited a much lower TEER of around 15 – 20 $\Omega \cdot cm^2$ at D8, while still expressing regular tight junction proteins. Similarly, another study found TEER values of 8 – 10 Ω·cm2 for their model of hCMEC/D3 mono- and co-cultures with U87MG cells, validating that stable cell lines produce a lower TEER as one of their characteristics (Kim, Shin et al. 2023). In addition, that same paper also reported a significantly higher TEER (**$p<0.01$) for

transwells of the 3 μm pore size group compared to 0.4 μm, which also played into the design of this study. Notably, the established *in vitro* model in this project has important physiological features of a barrier including consistent TEER, tight junction expression, a confluent monolayer of HBMECs, and a responsiveness to external stimuli, such as hypoxia and EDTA, making it a suitable model to investigate the BBB.

In HBMECs monolayers and BBB tri-cultures, which suffered from oxidative stress by hypoxic insult, PBM restored the barrier function almost back to the baseline levels at 24 and 48 hours post-treatment (Figure 5E & F). To understand whether this was driven by a PBM-mediated improvement in cell viability or reduction in cytotoxicity, two orthogonal assays based on ATP levels were conducted, which showed no statistical difference between groups. These findings indicated that there is a different favourable molecular response and structural arrangement of HBMECs upon PBM. Indeed, while ICC analysis of ZO-1 showed no difference in tight junction expression, its organisation seems to be less aberrant after hypoxia and closer to healthy HBMECs following PBM treatment (Figure 6C & F). A disrupted continuation and re-localisation of ZO-1 has been already reported *in vivo* as a pathological hallmark of hypoxia-induced vascular leakage (Bauer, Bürgers et al. 2009). Moreover, data showed the upregulation of the platelet-adhesion molecule vWF after endothelial injury and induced BBB permeability allowing for leukocyte infiltration (Suidan, De Meyer et al. 2010). Expression data of vWF revealed a significant downregulation upon PBM on a gene and protein level and a direct pathway involvement in improving the TEER by siRNA knockdown of vWF (Figure 16 & 17). A similar effect was found in another study where the impact of $vWF^{-/-}$ mice following hypoxia and reoxygenation was examined. There they discovered that vWF deficient mice portrayed a tighter BBB with less permeability that wild-type animals, supporting the findings of this project (Suidan, Brill et al. 2013). A similar effect of modulating pro-thrombotic factors was also observed upon the cytokine dot plot, where PBM significantly decreased PAI-1 of tri-cultures in normoxia and hypoxia (Figure 18D). PAI-1, encoded by *SerpinE1*, is known to be upregulated upon prosenescent stimuli favouring thrombosis, endothelial dysfunction, and

age-related morbidities (Vaughan, Rai et al. 2017). A recent study found a reduced BBB permeability and pro-inflammatory gene expression upon *SerpinE1* knockdown in mice subjected them to ischemic stroke compared to wild-type animals (Narayana, Lambert et al. 2025). Overall, these findings discovered PBM's anti-thrombotic effect on the BBB by modulating vWF and PAI-1 levels; findings of PBM that have not been reported yet.

The cytokine dot plot also revealed that PBM leads to the upregulation of the chemokines IL-8 and GROα, and cytokines IL-21, MIF, and GM-CSF (Figure 18). It has been shown that recombinant human IL-8 enhanced the proliferation of ECs, capillary tube organisation, and angiogenesis characterised by an upregulation of antiapoptotic markers (Li, Dubey et al. 2003). Interestingly, IL-8 expressed by ECs is stored in WPBs and closely correlated with the concentration of vWF (Bierings, Van Den Biggelaar et al. 2007). Since vWF is downregulated by PBM, that would mean that upregulation of IL-8 must be released by HAs and/or HVPCs which then influences the maintenance of HBMECs. This highlights the importance of the contact tri-culture model in this study and how the cell-specific modifications via PBM could improve the BBB health.

MIF is a pro-inflammatory cytokine and normally released by immune cells and human umbilical vein endothelial cells. While pro-inflammatory mechanisms are usually associated with damage, there has been proof of MIF's neuroprotective effect during ischemia and stroke (Zis, Zhang et al. 2015). This phenomenon was observed in two *in vivo* models subjected to middle cerebral artery occlusion or ligation where upregulation of MIF was directly linked to a reduced infarct volume, increase of neuroprotective factors such as the brain-derived neurotropic factor (BDNF), and inhibition of caspase-3 activation (Zhang, Zis et al. 2014, Kim, Kim et al. 2022). With PBM favouring MIF expression in tri-culture this could translate into a protective effect against neuronal cell death following hypoxia, one of the most severe consequences leading to cognitive impairment. Moreover, the activation of GM-CSF, a growth and differentiation factor, has also been shown to inhibit programmed cell death of primary cortical neurons and human neuroblastoma cells by

activating the antiapoptotic factors B-cell lymphoma-2 (Bcl-2) and B-cell lymphoma-extra-large (Bcl-xL) (Schäbitz, Krüger et al. 2007). GM-CSF treatment also increased the transepithelial resistance (by ~20% and ~30 – 40% respectively) of two *in vitro* transwell models of the lung with immortalised human bronchiolar epithelial cells and rat type II alveolar epithelial cells being subjected to TGF-β1(Overgaard, Schlingmann et al. 2015). Despite the misconception that the increase of cyto- and chemokines is automatically linked to damaging effects, here red and infrared light could lead to a neuroprotective effect and restoration of barrier function as discovered in prior studies. To test the neuroprotective effect of PBM through the modulation of MIF and GM-CSF, potential experiments could include an *in vitro* transwell model of the multicellular neurovascular unit where neurons are being cultured on the well plate or treating neurons with PBM-conditioned media from the BBB *in vitro* model.

The stabilisation of HIF-1α is one of the earliest cellular responses during hypoxia and is in close relationship with ROS synthesis. Yet, as suggested in our results (Figure 13 & 15), HIF-1α regulation can also occur independently of ROS (Lee, Chandel and Simon 2020). Here PBM significantly reduced ROS levels in HAs and HVPCs while HIF-1α gene and protein expression remained unchanged. On the contrary, ROS production was unaffected by light irradiation in HBMECs yet HIF-1α was statistically downregulated detected by ICC. These interesting findings emphasise the cell-specific responses to PBM and also complementarily reflects its therapeutic effect. Previous studies suggested a direct link between HIF-1α in ECs and the BBB disruption by demonstrating an improved barrier integrity upon HIF-1α inhibition. Thus, downregulating HIF-1α, modulating ROS levels, and boosting mitochondrial function in ECs could support the maintenance of tight junctions and barrier integrity following hypoxia (Engelhardt, Patkar and Ogunshola 2014).

The OCR results showed that the basal respiration in HBMECs and HAs was strongly impaired at 24 hours after hypoxia. Literature suggests that hypoxic cells switch to glycolysis upon mitochondrial dysfunction. Yet, the results from the basal glycolytic rate at 24 hours after hypoxia

(Figure 12A, E, & I) did not differ to the ECAR of cells incubated in normoxia. This implies that since their glycolytic rate is unchanged hypoxic cells do rely on glycolysis to receive energy. Therefore, the drop in basal OCR might be an acute reaction to hypoxia, HIF-1α upregulation, or cell death since their basal respiration recovered after 48 hours (Figure 9). In addition, the proton leak of all cells did not rise at 24 hours after being exposed to hypoxia (Figure 10B, F, & J) which is an interesting finding as it suggests, that there might be limited/no membrane damage or compromised integrity, but rather a downregulation of mitochondrial oxidative capacity and less activity. This reduced capacity was found to be significantly boosted by PBM in HBMECs. At 24 hours after hypoxia, PBM-treated HBMECs showed an increased maximal respiration compared to non-PBM hypoxic cells (Figure 10C). This translates into an enhanced electron transport chain efficiency and mitochondrial capacity upon PBM, which are normally impaired after hypoxia. Indeed, this finding supports the hypothesis, that PBM dissociates NO from the CCO leaving an open binding site for O_2 to boost mitochondrial respiration (Beltrán, Mathur et al. 2000). To confirm this direct connection, the PBM-mediated release of NO levels after hypoxia could be detected via a NO electrode or fluorescent NO indicator DAF-FM (4-amino-5-methylamino-2′,7′-difluorofluorescein diacetate), as NO is extremely instable (Tjalkens, Carbone and Wu 2011).

Taken together, this project addresses the objectives and an important knowledge gap by identifying molecular players and changes in cell behaviour through which PBM supports recovery of BBB function following hypoxic stress. Moreover, the BBB was successfully modelled *in vitro* using human cell lines cultured on the transwell system with physiologically relevant features including a confluent monolayer, cell-to-cell talk, and ZO-1 expression. The use of immortalised cell lines enabled the generation of a robust and reproducible BBB model within the available timeframe and ensured sufficient cell numbers for functional assays. However, this choice necessarily places some constraints on the depth of transcriptomic and proteomic interrogation. As immortalisation via SV40 large T antigen can influence cell-cycle regulation and senescence pathways, future studies using induced pluripotent stem cell–derived BBB cell types would be well suited to extend these findings

and explore the underlying molecular programmes in greater detail. The static transwell model also lacks a shear flow found in blood vessels which changes the morphology and dynamics of cells. Another factor to consider, is that while the PBM-source used in this study is commercially available, its wavelengths and power are fixed. Therefore, it was not possible to detect which wavelength and power trigger the cell-specific changes of the BBB. In transcranial PBM the light penetration is obstructed by multiple layers of the head including the meninges and skull bone, which was also not assessed in this project. Despite the limitations of the project, PBM has a favourable safety profile and offers a non-invasive approach to targeting BBB dysfunction (Enengl, Hamblin et al. 2020). This is particularly relevant given that therapeutic strategies that improve the cerebrovascular health are limited and current monoclonal antibodies or small molecule treatments exhibit systemic side effects like urinary tract infection, insomnia, and muscle weakness (Lemarchant, Engelhardt et al. 2025). LLLT therefore has the potential to shift how cerebrovascular damage is addressed, upon acute neurological incidences such as stroke or TBI, but also in chronic disorders where prolonged hypoxia contributed to progressive BBB impairment.

6. LIST OF TABLES

Table 1: Cell count of seeded HAs, HBMECs, and HVPCs per 24-well transwell insert (cells/insert) for all cultured transwell models. 23

Table 2: Cell culture media for apical and basal chamber for each transwell culture. 24

Table 3: Properties of each LED light found in the toprwap TW-03B for one session lasting 5 minutes. 27

Table 4: Primary and secondary antibodies used for staining of HBMECs, HVPCs, and HAs. 32

Table 5: Forward and reverse sequences for all primers used in 5' to 3'. 34

Table 6: Forward and reverse sequences of housekeeping genes in 5' to 3' that were screened including the literature source. 35

7. LIST OF FIGURES

Figure 1: Cellular architecture of the BBB and the junctional proteins contributing to the tightness of endothelial cells at the BBB. Created with Biorender. Adapted from Yang, Wang et al. 2023. 10

Figure 2: Illustration of (A) the cultured in vitro transwell models, to understand cell-to-cell communication, and (B) the coating and seeding of a tri-culture model. Created with Biorender. 24

Figure 3: LED lights and dimensions of the topwrap TW-03B from ProNeuroLight used for the PBM treatments. Created with Biorender. 27

Figure 4: Identification of HK gene with the (A) CT values and (B) mean standard deviation (SD) for each gene. The highest variability was observed for GAPDH, PPIA, and RRP1, whereas the RPL13A had the lowest SD values. 35

*Figure 5: (A) Timeline of seeding the transwell model, exposure to groups, and follow-up analysis. Created with Biorender. (B) Quantification of the coating optimisation of the transwell model shown as the change of relative TEER for PLL, Matrigel, and GelTrex coating with the TEER normalised to the uncoated transwell. Two-way ANOVA (Tukey's multiple comparison test) with *p<0.05, **p<0.01 and n=2 (technical replicates). (C) Assessment of barrier function, shown as the change in relative TEER (%) at 48 hours post normoxia. (D) The impact of hypoxia (6 hours at 1% O_2) on the BBB function assessed by the drop in relative TEER. Assessment of barrier function at (E) 24 hours post hypoxia, and (F) 48 hours post hypoxia. Multiple unpaired t-test (Holm-Sidak methods) with *p<0.05 and N=4 (biological replicates). Error bars represent mean +/- SEM. EC: HBMEC monoculture; EC+AC: HBMEC/HA co-culture; EC+PC: HBMEC/HVPC co-culture; Tri: Tri-culture; EDTA: EDTA-treated tri-culture as negative control. 44*

Figure 6: Expression of ZO-1 in (A-C) normoxia and (D-F) hypoxia. Fold change of ZO-1 RNA expression in (A) normoxia and (D) hypoxia groups. Quantification of ZO-1 protein expression from ICC, with the area of ZO-1 normalised to the area of DAPI, in (B) normoxia and (E) hypoxia groups. ICC images of ZO-1 (magenta) and DAPI (blue) in (C) normoxia and (F) hypoxia groups. Unpaired t-test with N=3-4 (biological replicates). Error bars represent mean +/- SEM. 46

List of Figures

Figure 7: Quantification of the cell viability as the fluorescence signal (%) relative to the baseline signal after 48 hours for (A) normoxia and (B) hypoxia groups. (C) Quantification of the cytotoxicity as the relative luminescence signal (%) at 48 hours post hypoxia. Multiple unpaired t-test (Holm-Sidak methods) with N=4 (biological replicates). Error bars represent mean +/- SEM. EC: HBMEC monoculture; AC: HA monoculture; PC: HVPC monoculture; Tri: Tri-culture; EDTA: EDTA-treated tri-culture as negative control. *47*

Figure 8: The apparent permeability (cm/s) at 48 hours in (A) normoxia and (B) hypoxia groups. Multiple unpaired t-test (Holm-Sidak methods) with N=4 (biological replicates). Error bars represent mean +/- SEM. EC: HBMEC monoculture; AC: HA monoculture; PC: HVPC monoculture; Tri: Tri-culture; EDTA: EDTA-treated tri-culture as negative control. *47*

*Figure 9: Assessment of the OCR in HBMECs, HAs, and HVPCs at 24 hours (A, E, I) and at 48 hours (C, G, K) respectively. OCR (%) was normalised to protein concentration and to the basal OCR for all four conditions. The basal respiration (pmol/min/µg protein) was calculated before oligomycin injection for all conditions in HBMECs, HAs, and HVPCs at 24 hours (B, F, J) and at 48 hours (D, H, L) respectively. One-way ANOVA (Tukey's multiple comparisons test) with *p<0.05, **p<0.01, ***p<0.001 and N=4 (biological replicates). Error bars represent mean +/- SEM.* *50*

*Figure 10: Quantification of the fold change of the (A, E, I) ATP production, (B, F, J) proton leak, (C, G, K) maximal respiration, and (D, H, L) spare capacity at 24 hours, after normalisation to % of the basal OCR respiration, in (A-D) HBMECs, (E-H) HAs, and (I-L) HVPCs. The ATP production was calculated as the difference of basal respiration and the oligomycin injection. The proton leak was calculated as the measurements after oligomycin injection. The maximal respiration was calculated as the measurements after FCCP injection. The spare capacity was calculated as the difference between the maximal and basal respiration. The non-mitochondrial respiration was calculated as the measurements after R/A and subtracted from all OCR stages. One-way ANOVA (Tukey's multiple comparisons test) with *p<0.05 and N=4 (biological replicates). Error bars represent mean +/- SEM.* *51*

Figure 11: Quantification of the fold change of the (A, E, I) ATP production, (B, F, J) proton leak, (C, G, K) maximal respiration, and (D, H, L) spare capacity at 48 hours, after normalisation to % of the basal OCR respiration, in (A-D) HBMECs, (E-H) HAs, and (I-L) HVPCs. The ATP production was calculated as

*the difference of basal respiration and the oligomycin injection. The proton leak was calculated as the measurements after oligomycin injection. The maximal respiration was calculated as the measurements after FCCP injection. The spare capacity was calculated as the difference between the maximal and basal respiration. The non-mitochondrial respiration was calculated as the measurements after R/A and subtracted from all OCR stages. One-way ANOVA (Tukey's multiple comparisons test) with *p<0.05 and N=4 (biological replicates). Error bars represent mean +/- SEM. 52*

*Figure 12: The glycolytic ECAR (mpH/min/µg protein) was calculated as a measurement before oligomycin injection for all four conditions in HBMECs, HAs, and HVPCs at 24 hours (A, E, I) and at 48 hours (C, G, K) respectively. Quantification of the fold change of the reserved glycolytic capacity at (B, F, J) at 24 hours and (D, H, L) at 48 hours respectively. The reserved glycolytic capacity was calculated as the difference of glycolytic ECAR and the oligomycin injection. One-way ANOVA (Tukey's multiple comparisons test) with *p<0.05, **p<0.01 and N=4 (biological replicates). Error bars represent mean +/- SEM. 54*

*Figure 13: Quantification of ROS levels in (A-C) normoxia and (D-F) hypoxia. (A-C) Average luminescence signal in (A) HBMECs, (B) HAs, and (C) HVPCs. (D-F) Average luminescence signal in (D) HBMECs, (E) HAs, and (F) HVPCs. One-way ANOVA (Tukey's multiple comparisons test) with *p<0.05, **p<0.01 and N=4 (biological replicates). Error bars represent mean +/- SEM..... 56*

Figure 14: Expression of HIF-1α in normoxia in (A-C) HBMECs, (D-F) HAs, and (G-I) HVPCs. (A, D, G) Fold change of HIF-1α RNA expression in (A) HBMECs, (D) HAs, and (G) HVPCs. Quantification of HIF-1α protein expression, with the mean intensity normalised to the area of DAPI, in (B) HBMECs, (E) HAs, and (H) HVPCs. ICC images of HIF-1α (cyan) and DAPI (blue) in (C) HBMECs, (F) HAs, and (I) HVPCs. Unpaired t-test with N=3-4 (biological replicates). Error bars represent mean +/- SEM..... 57

*Figure 15: Expression of HIF-1α post hypoxia in (A-C) HBMECs, (D-F) HAs, and (G-I) HVPCs. (A, D, G) Fold change of HIF-1α RNA expression in (A) HBMECs, (D) HAs, and (G) HVPCs. Quantification of HIF-1α protein expression, with the mean intensity normalised to the area of DAPI, in (B) HBMECs, (E) HAs, and (H) HVPCs. ICC images of HIF-1α (cyan) and DAPI (blue) in (C) HBMECs, (F) HAs, and (I) HVPCs. Unpaired t-test with *p<0.05 and N=3-4 (biological replicates). Error bars represent mean +/- SEM.. 58*

List of Figures

*Figure 16: Expression of vWF in (B-C) normoxia and (D-E) hypoxia. (A) Fold change of vWF RNA expression for all groups. One-way ANOVA (Tukey's multiple comparisons test) with ****p<0.0001 and N=3-4 (biological replicates). Quantification of vWF protein expression, with the mean intensity normalised to the area of DAPI, in (B) normoxia and (D) hypoxia groups. Unpaired t-test with N=3 (biological replicates). ICC images of ZO-1 (magenta) and DAPI (blue) in (C) normoxia and (E) hypoxia groups. Error bars represent mean +/- SEM. 59*

*Figure 17: (A) RNA expression of vWF in wild-type and siRNA-treated HBMECs. Unpaired t-test with ****p<0.0001 and N=8 (biological replicates). Assessment of barrier function, shown as the change in relative TEER (%) at 24 and 48 hours (B) in normoxia and (C) post hypoxia. Multiple unpaired t-test (Holm-Sidak methods) with N=4 (biological replicates). Error bars represent mean +/- SEM. EC: HBMEC monoculture; Tri: Tri-culture; EDTA: EDTA-treated tri-culture as negative control. 60*

*Figure 18: (A) Representative image from the iBright imager of positive and significant markers from the Proteome Profiler Human Cytokine Array. The intensity of two dots per group was averaged and the background intensity subtracted. Relative expression levels were normalised to the untreated normoxia group of (B) IL-8, (C) IL-21, (D) Serpin E1/PAI-1, (E) CXCL/GROα, (F) GM-CSF, and (G) MIF. Unpaired t-test with *p<0.05, **p<0.01, ***p<0.001 and n=2 (technical replicates). Error bars represent mean +/- SEM. 62*

Figure 19: Expression of AQP4 in (B-C) normoxia and (D-E) hypoxia. (A) Fold change of AQP4 RNA expression for all groups. One-way ANOVA (Tukey's multiple comparisons test) with N=5 (biological replicates). Quantification of AQP4 protein expression, with the mean intensity normalised to the area of DAPI, in (B) normoxia and (D) hypoxia groups. Unpaired t-test with N=3 (biological replicates). ICC images of AQP4 (grey) and DAPI (blue) in (C) normoxia and (E) hypoxia groups. Error bars represent mean +/- SEM. 63

Figure 20: (A) Example of live-cell images to assess HAs cell swelling with calcein (green) and DAPI (blue) for hypoxia groups and the untreated normoxia group (control). (B) Quantification of cell swelling, with the mean area normalised to the DAPI cell count. One-way ANOVA (Tukey's multiple comparisons test) with N=3 (biological replicates). Error bars represent mean +/- SEM. 64

List of Figures

Figure 21: Expression of GFAP in (B-C) normoxia and (D-E) hypoxia. (A) Fold change of GFAP RNA expression for all groups. One-way ANOVA (Tukey's multiple comparisons test) with N=5 (biological replicates). Quantification of GFAP protein expression, with the mean intensity normalised to the area of DAPI, in (B) normoxia and (D) hypoxia groups. Unpaired t-test with N=3 (biological replicates). ICC images of GFAP (magenta) and DAPI (blue) in (C) normoxia and (E) hypoxia groups. Error bars represent mean +/- SEM. *65*

Figure 22: Expression of PDGFRβ in (B-C) normoxia and (D-E) hypoxia. (A) Fold change of Rgs5 RNA expression for all groups. One-way ANOVA (Tukey's multiple comparisons test) with N=5 (biological replicates). Quantification of PDGFRβ protein expression, with the mean intensity normalised to the area of DAPI, in (B) normoxia and (D) hypoxia groups. Unpaired t-test with N=3 (biological replicates). ICC images of PDGFRβ (grey) and DAPI (blue) in (C) normoxia and (E) hypoxia groups. Error bars represent mean +/- SEM. *66*

Figure 23: Expression of Actin in (B-C) normoxia and (D-E) hypoxia. (A) Fold change of αSMA RNA expression for all groups. One-way ANOVA (Tukey's multiple comparisons test) with N=5 (biological replicates). Quantification of Actin protein expression, with the mean intensity normalised to the area of DAPI, in (B) normoxia and (D) hypoxia groups. Unpaired t-test with N=3 (biological replicates). ICC images of Actin (magenta) and DAPI (blue) in (C) normoxia and (E) hypoxia groups. Error bars represent mean +/- SEM. *67*

8. REFERENCES

Andjelkovic, A. V., M. Situ, A. F. Citalan-Madrid, S. M. Stamatovic, J. Xiang and R. F. Keep (2023). "Blood-Brain Barrier Dysfunction in Normal Aging and Neurodegeneration: Mechanisms, Impact, and Treatments." Stroke **54**(3): 661-672.

Ansbro, M. R., S. Shukla, S. V. Ambudkar, S. H. Yuspa and L. Li (2013). "Screening compounds with a novel high-throughput ABCB1-mediated efflux assay identifies drugs with known therapeutic targets at risk for multidrug resistance interference." PLoS One **8**(4): e60334.

Araque, A., V. Parpura, R. P. Sanzgiri and P. G. Haydon (1999). "Tripartite synapses: glia, the unacknowledged partner." Trends in Neurosciences **22**(5): 208-215.

Barberio, C., A. Withers, Y. Mishra, P.-O. Couraud, I. A. Romero, B. Weksler and R. M. Owens (2022). "A human-derived neurovascular unit in vitro model to study the effects of cellular cross-talk and soluble factors on barrier integrity." Frontiers in Cellular Neuroscience **Volume 16 - 2022**.

Bauer, A. T., H. F. Bürgers, T. Rabie and H. H. Marti (2009). "Matrix Metalloproteinase-9 Mediates Hypoxia-Induced Vascular Leakage in the Brain via Tight Junction Rearrangement." Journal of Cerebral Blood Flow & Metabolism **30**(4): 837-848.

Beltrán, B., A. Mathur, M. R. Duchen, J. D. Erusalimsky and S. Moncada (2000). "The effect of nitric oxide on cell respiration: A key to understanding its role in cell survival or death." Proceedings of the National Academy of Sciences **97**(26): 14602-14607.

Bierings, R., M. Van Den Biggelaar, A. Kragt, K. Mertens, J. Voorberg and J. A. Van Mourik (2007). "Efficiency of von Willebrand factor-mediated targeting of interleukin-8 into Weibel–Palade bodies." Journal of Thrombosis and Haemostasis **5**(12): 2512-2519.

Cader, Z. (2022). Human Blood-Brain-Barrier In Vitro Models: Overview and Applications. Physiology, Pharmacology and Pathology of the Blood-Brain Barrier. Z. Cader and W. Neuhaus. Cham, Springer International Publishing**:** 205-222.

Carlsson, R., A. Enström and G. Paul (2023) "Molecular Regulation of the Response of Brain Pericytes to Hypoxia." International Journal of Molecular Sciences **24**, 5671 DOI: 10.3390/ijms24065671.

References

Chamkouri, H. and L. Chen (2025). "Advancement of Photobiomodulation Therapy Using 680 and 850 nm Light-Emitting Diodes for the Differentiation of Human Brain Endothelial Cells." Advanced Therapeutics **8**(9): e00164.

Chaudary, S., L. Karner, A. Weidinger, B. Meixner, S. Rieger, M. Metzger, J. Zipperle and P. Dungel (2020). "In vitro effects of 635 nm photobiomodulation under hypoxia/reoxygenation culture conditions." J Photochem Photobiol B **209**: 111935.

Colombo, E., A. Signore, S. Aicardi, A. Zekiy, A. Utyuzh, S. Benedicenti and A. Amaroli (2021) "Experimental and Clinical Applications of Red and Near-Infrared Photobiomodulation on Endothelial Dysfunction: A Review." Biomedicines **9**, 274 DOI: 10.3390/biomedicines9030274.

Dunn, J. F. and A. M. Isaacs (2021). "The impact of hypoxia on blood-brain, blood-CSF, and CSF-brain barriers." Journal of Applied Physiology **131**(3): 977-985.

Enengl, J., M. R. Hamblin, P. Dungel and J. Peter (2020). "Photobiomodulation for Alzheimer's Disease: Translating Basic Research to Clinical Application." Journal of Alzheimer's Disease **75**(4): 1073-1082.

Engelhardt, S., S. Patkar and O. O. Ogunshola (2014). "Cell-specific blood–brain barrier regulation in health and disease: a focus on hypoxia." British Journal of Pharmacology **171**(5): 1210-1230.

Gokce, C., B. Altun, E. Kirit, H. Yavuz, R. Uyar, D. Celik and A. Yilmazer (2025). "Unlocking the human blood-brain barrier (BBB) characteristics for the development of nano-delivery strategies for central nervous system therapies." Journal of Drug Delivery Science and Technology **108**: 106961.

Hayashi, K., S. Nakao, R. Nakaoke, S. Nakagawa, N. Kitagawa and M. Niwa (2004). "Effects of hypoxia on endothelial/pericytic co-culture model of the blood-brain barrier." Regul Pept **123**(1-3): 77-83.

Helms, H. C., N. J. Abbott, M. Burek, R. Cecchelli, P.-O. Couraud, M. A. Deli, C. Förster, H. J. Galla, I. A. Romero, E. V. Shusta, M. J. Stebbins, E. Vandenhaute, B. Weksler and B. Brodin (2016). "In vitro models of the blood–brain barrier: An overview of commonly used brain endothelial cell culture models and guidelines for their use." Journal of Cerebral Blood Flow & Metabolism **36**(5): 862-890.

Hennessy, M. and M. R. Hamblin (2017). "Photobiomodulation and the brain: a new paradigm." Journal of Optics **19**(1): 013003.

Hipskind, S. G., F. L. Grover, Jr., T. R. Fort, D. Helffenstein, T. J. Burke, S. A. Quint, G. Bussiere, M. Stone and T. Hurtado (2019). "Pulsed Transcranial Red/Near-Infrared Light Therapy Using Light-Emitting Diodes Improves Cerebral Blood Flow and Cognitive Function in Veterans with Chronic Traumatic Brain Injury: A Case Series." Photobiomodul Photomed Laser Surg **37**(2): 77-84.

Huang, Z., M. R. Hamblin and Q. Zhang (2024). "Photobiomodulation in experimental models of Alzheimer's disease: state-of-the-art and translational perspectives." Alzheimer's Research & Therapy **16**(1): 114.

Kawecki, C., P. J. Lenting and C. V. Denis (2017). "von Willebrand factor and inflammation." Journal of Thrombosis and Haemostasis **15**(7): 1285-1294.

Kim, J., S. A. Shin, C. S. Lee and H. J. Chung (2023). "An Improved In Vitro Blood-Brain Barrier Model for the Evaluation of Drug Permeability Using Transwell with Shear Stress." Pharmaceutics **16**(1).

Kim, J.-w., I. Tchernyshyov, G. L. Semenza and C. V. Dang (2006). "HIF-1-mediated expression of pyruvate dehydrogenase kinase: A metabolic switch required for cellular adaptation to hypoxia." Cell Metabolism **3**(3): 177-185.

Kim, J. A., Y. Y. Kim, S. H. Lee, C. Jung, M. H. Kim and D. Y. Kim (2022). "Neuroprotective Effect of Macrophage Migration Inhibitory Factor (MIF) in a Mouse Model of Ischemic Stroke." International Journal of Molecular Sciences **23**(13): 6975.

Kutikhin, A. G., D. K. Shishkova, E. A. Velikanova, M. Y. Sinitsky, A. V. Sinitskaya and V. E. Markova (2022). "Endothelial Dysfunction in the Context of Blood–Brain Barrier Modeling." Journal of Evolutionary Biochemistry and Physiology **58**(3): 781-806.

Lee, P., N. S. Chandel and M. C. Simon (2020). "Cellular adaptation to hypoxia through hypoxia inducible factors and beyond." Nature Reviews Molecular Cell Biology **21**(5): 268-283.

Lemarchant, S., B. Engelhardt, F. Cicchetti, G. J. Bix, A. Janus, Y. Godfrin, H. Blasco, M. Campbell and A. de Rus Jacquet (2025). "Restoring brain barriers: an innovative approach for treating neurological disorders." Fluids Barriers CNS **22**(1): 72.

Li, A., S. Dubey, M. L. Varney, B. J. Dave and R. K. Singh (2003). "IL-8 directly enhanced endothelial cell survival, proliferation, and matrix metalloproteinases production and regulated angiogenesis." J Immunol **170**(6): 3369-3376.

Liebner, S., R. M. Dijkhuizen, Y. Reiss, K. H. Plate, D. Agalliu and G. Constantin (2018). "Functional morphology of the blood-brain barrier in health and disease." Acta Neuropathol **135**(3): 311-336.

Ma, C., Y. Ye, X. Shi, N. Li, Z. Mu, T. Tan, H. Yin, J. Dai, Y. Liu and H. Chen (2025). "Photobiomodulation mitigates blood–brain barrier disruption in APP/PS1 mouse model of Alzheimer's disease by activating the AMPK pathway." Alzheimer's Research & Therapy **17**(1): 141.

Mastorakos, P. and D. McGavern (2019). "The anatomy and immunology of vasculature in the central nervous system." Science Immunology **4**(37): eaav0492.

Merelli, A., J. C. G. Rodríguez, J. Folch, M. R. Regueiro, A. Camins and A. Lazarowski (2018). "Understanding the Role of Hypoxia Inducible Factor During Neurodegeneration for New Therapeutics Opportunities." Curr Neuropharmacol **16**(10): 1484-1498.

Nagelhus, E. A. and O. P. Ottersen (2013). "Physiological roles of aquaporin-4 in brain." Physiol Rev **93**(4): 1543-1562.

Narayana, K., I. C. Lambert, S. Burford, E. Gosselin, J. Körbelin and C. E. Brown (2025). "Knockdown of endothelial Serpine1 improves stroke recovery by attenuating peri-infarct blood flow and blood brain barrier disruption." bioRxiv: 2025.2010.2015.682687.

Ogunshola, O. O. and A. Al-Ahmad (2012). "HIF-1 at the Blood-Brain Barrier: A Mediator of Permeability?" High Altitude Medicine & Biology **13**(3): 153-161.

Overgaard, C. E., B. Schlingmann, S. Dorsainvil White, C. Ward, X. Fan, S. Swarnakar, L. A. S. Brown, D. M. Guidot and M. Koval (2015). "The relative balance of GM-CSF and TGF-β1 regulates lung epithelial barrier function." American Journal of Physiology-Lung Cellular and Molecular Physiology **308**(12): L1212-L1223.

Profaci, C. P., R. N. Munji, R. S. Pulido and R. Daneman (2020). "The blood–brain barrier in health and disease: Important unanswered questions." Journal of Experimental Medicine **217**(4).

Roberts, W. G., J. Delaat, M. Nagane, S. Huang, W. K. Cavenee and G. E. Palade (1998). "Host microvasculature influence on tumor vascular morphology and endothelial gene expression." Am J Pathol **153**(4): 1239-1248.

Rust, R., H. Yin, B. Achón Buil, A. P. Sagare and K. Kisler (2025). "The blood–brain barrier: a help and a hindrance." Brain **148**(7): 2262-2282.

Salman, M. M., P. Kitchen, A. Halsey, M. X. Wang, S. Törnroth-Horsefield, A. C. Conner, J. Badaut, J. J. Iliff and R. M. Bill (2022). "Emerging roles for dynamic aquaporin-4 subcellular relocalization in CNS water homeostasis." Brain **145**(1): 64-75.

Schäbitz, W.-R., C. Krüger, C. Pitzer, D. Weber, R. Laage, N. Gassler, J. Aronowski, W. Mier, F. Kirsch, T. Dittgen, A. Bach, C. Sommer and A. Schneider (2007). "A Neuroprotective Function for the Hematopoietic Protein Granulocyte-Macrophage Colony Stimulating Factor (GM-CSF)." Journal of Cerebral Blood Flow & Metabolism **28**(1): 29-43.

Simöes Da Gama, C. and M. Morin-Brureau (2022). "Study of BBB Dysregulation in Neuropathogenicity Using Integrative Human Model of Blood–Brain Barrier." Frontiers in Cellular Neuroscience **Volume 16 - 2022**.

Srinivasan, B. and A. R. Kolli (2025). Transepithelial/Transendothelial Electrical Resistance (TEER) to Measure the Integrity of Blood-Brain Barrier. Blood-Brain Barrier. T. Barichello. New York, NY, Springer US**:** 127-144.

Staelens, M., E. Di Gregorio, A. P. Kalra, H. T. Le, N. Hosseinkhah, M. Karimpoor, L. Lim and J. A. Tuszyński (2022). "Near-Infrared Photobiomodulation of Living Cells, Tubulin, and Microtubules In Vitro." Frontiers in Medical Technology **Volume 4 - 2022**.

Suidan, G. L., A. Brill, S. F. De Meyer, J. R. Voorhees, S. M. Cifuni, J. E. Cabral and D. D. Wagner (2013). "Endothelial Von Willebrand Factor Promotes Blood–Brain Barrier Flexibility and Provides Protection From Hypoxia and Seizures in Mice." Arteriosclerosis, Thrombosis, and Vascular Biology **33**(9): 2112-2120.

Suidan, G. L., S. F. De Meyer, A. Brill, S. M. Cifuni and D. D. Wagner (2010). "The Role of VWF In BBB Permeability Associated with Hypoxia/Reoxygenation." Blood **116**(21): 2102.

Tjalkens, R. B., D. L. Carbone and G. Wu (2011). "Detection of nitric oxide formation in primary neural cells and tissues." Methods Mol Biol **758**: 267-277.

Vaughan, D. E., R. Rai, S. S. Khan, M. Eren and A. K. Ghosh (2017). "Plasminogen Activator Inhibitor-1 Is a Marker and a Mediator of Senescence." Arteriosclerosis, Thrombosis, and Vascular Biology **37**(8): 1446-1452.

References

Verkman, A. S., P. W. Phuan, N. Asavapanumas and L. Tradtrantip (2013). "Biology of AQP4 and anti-AQP4 antibody: therapeutic implications for NMO." Brain Pathol **23**(6): 684-695.

Waithe, O. l. Y., X. Peng, E. W. Childs and B. Tharakan (2024). Measurement of Transendothelial Electrical Resistance in Blood-Brain Barrier Endothelial Cells. Vascular Hyperpermeability: Methods and Protocols. B. Tharakan. New York, NY, Springer US**:** 199-203.

Winter, R., P. Dungel, F. M. J. Reischies, S. Rohringer, P. Slezak, C. Smolle, S. Spendel, L.-P. Kamolz, N. Ghaffari-Tabrizi-Wizsy and K. Schicho (2018). "Photobiomodulation (PBM) promotes angiogenesis in-vitro and in chick embryo chorioallantoic membrane model." Scientific Reports **8**(1): 17080.

Wu, D., Q. Chen, X. Chen, F. Han, Z. Chen and Y. Wang (2023). "The blood–brain barrier: Structure, regulation and drug delivery." Signal Transduction and Targeted Therapy **8**(1): 217.

Yan, B., J. Zhou, F. Yan, M. Gao, J. Tang, L. Huang and Y. Luo (2025). "Unlocking the potential of photobiomodulation therapy for brain neurovascular coupling: The biological effects and medical applications." Journal of Cerebral Blood Flow & Metabolism **45**(5): 800-830.

Yosef, N., Y. Xi and J. H. McCarty (2020). "Isolation and transcriptional characterization of mouse perivascular astrocytes." PLoS One **15**(10): e0240035.

Zhang, S., O. Zis, P. T. Ly, Y. Wu, S. Zhang, M. Zhang, F. Cai, R. Bucala, W. C. Shyu and W. Song (2014). "Down-regulation of MIF by NFκB under hypoxia accelerated neuronal loss during stroke." Faseb j **28**(10): 4394-4407.

Zhou, T., T. Y. Ohulchanskyy and J. Qu (2021). "Effect of NIR light on the permeability of the blood-brain barriers in in vitro models." Biomedical Optics Express **12**(12): 7544-7555.

Zis, O., S. Zhang, K. Dorovini-Zis, L. Wang and W. Song (2015). "Hypoxia Signaling Regulates Macrophage Migration Inhibitory Factor (MIF) Expression in Stroke." Molecular Neurobiology **51**(1): 155-167.